In compliance with the
Canadian Privacy Legislation
some supporting forms
may have been removed from
this dissertation.

While these forms may be included
in the document page count,
their removal does not represent
any loss of content from the dissertation.

Magnetization transfer imaging of multiple sclerosis

Ives Levesque

Medical Physics Unit

McGill University, Montreal

December, 2002

A thesis submitted to McGill University in partial fulfillment of the requirements of the degree of Master of Science.

Your file Votre référence
ISBN: 0-612-88245-4
Our file Notre référence
ISBN: 0-612-88245-4

Abstract

MAGNETIZATION transfer (MT) imaging is a magnetic resonance imaging technique which permits indirect observation of the macromolecular component of biological tissue. Semi-quantitative implementations such as magnetization transfer ratio (MTR) imaging are very useful in the study of neuro-degenerative diseases, despite the relatively limited information provided by such single measurement methods. Quantitative techniques provide estimated measures of model parameters that more accurately describe the MT process. This thesis presents the application of quantitative MT imaging in a cross-sectional study of multiple sclerosis (MS) patients and healthy controls, exploring the on-going changes that occur in MS. Quantitative results are investigated to determine which model parameters play a role in the MTR. The findings demonstrate regional variations in white matter structures, and significant differences between healthy and normal-appearing MS tissue. The results also indicate the dominant role of macromolecular content in MTR, and confirm the destructive nature of T_1-hypointense lesions.

Résumé

L'IMAGERIE par transfert de magnétisation (TM) est une technique d'imagerie par résonance magnétique qui permet d'observer indirectement les composantes macromoléculaire de tissus biologiques. Les applications semi-quantitatives, tel le ratio de transfert de magnétisation (RTM), sont très utiles dans l'étude de maladies neuro-dégénératives, malgré l'information limitée pourvue par de telles techniques à paramètre unique. Les méthodes quantitatives permettent de mesurer d'autres paramètres qui décrivent le procédé de TM de facon plus complète. Ce mémoire présente une application de l'imagerie quantitative par TM, dans une étude inter-patient transversale se penchant sur les changements qui surviennent dans les patients atteints de sclérose en plaques (SP). Les résultats quantitatifs sont analysés afin de déterminer quels paramètres jouent un rôle dans le RTM. Les observations démontrent des variations régionales dans la matière blanche, ainsi que des différences significatives entre la matière blanche "normale" des patients de SP et celle de contrôles. Les résultats indiquent aussi que la fraction macromoléculaire joue un rôle dominant dans le RTM, et confirment la nature destructive des lésions hypointenses sur les images T_1.

Acknowledgments

I WOULD like to thank Drs. Antonio Carlos Santos and Steven Brass for their help in collecting data; Simon Francis for his contribution of automatic tissue classification; Sridar Narayanan, Zografos 'Aki' Caramanos, and Dr. Doug Arnold for sharing their expertise in the field of multiple sclerosis; as well as Margery Knewstubb and Jennifer Chew for their administrative work. "Merci" to my colourful colleagues in the MRI and neighbouring labs – Peter, Marg, Najmom, Jennifer, Bojana, Mallar, Aki, Duche – for their help, and for providing a wonderful environment in which to do (or not to do?) work. Many thanks go to my family, for their encouragement and understanding.

Most importantly, I am very grateful to my advisor Dr. Bruce Pike, and to Dr. John Sled. Their work developed the entire set of tools used throughout this work. Without their invaluable collaboration and guidance, this project would not have been possible.

In addition, I would like to acknowledge financial support received from the Natural Sciences and Engineering Research Council of Canada (NSERC), and the Canadian Institutes for Health Research (CIHR).

Contents

List of figures

List of tables

Glossary

CNS	central nervous system
(C)SE	(conventional) spin-echo
CSF	cerebro-spinal fluid
EDSS	expanded disability status scale
FOV	field of view
GE	gradient echo
MRI	magnetic resonance imaging
MS	multiple sclerosis
MT(R)	magnetization transfer (ratio)
MTSPGR	magnetization transfer spoiled gradient (echo)
NAWM	normal-appearing white matter
NMR	nuclear magnetic resonance
PD	proton density
qMTI	quantitative magnetization transfer imaging
RF	radio frequency
ROI	region of interest
SNR	signal-to-noise ratio
TE	echo time
TR	repetition time
TSE	turbo spin echo

f	semi-solid/liquid pool ratio
k_f	forward magnetization exchange rate
PD_r, PD_f	free and restricted pool proton densities
T_1	spin-lattice relaxation time
T_2	spin-spin relaxation time
T_2^*	transverse relaxation time
$T_{1,f}$, $T_{2,f}$	free pool spin-lattice and spin-spin relaxation times
$T_{1,r}$, $T_{2,r}$	restricted pool spin-lattice and spin-spin relaxation times

"A proof is a proof. What kind of a proof? It's a proof. A proof is a proof. And when you have a good proof, it's because it's proven."

Jean Chrétien

Chapter 1

Introduction

MAGNETIC RESONANCE IMAGING (MRI) is a powerful means of studying normal function, disorder, and pathology of the central nervous system. Over the past decade it has become an important tool in the study of neuro-degenerative diseases, notably in multiple sclerosis (MS). T_2-weighted MRI has revealed itself to be very sensitive to MS lesions, but poor at differentiating between tissue breakdown and edema. T_1-weighted MRI has revealed focal pathology believed to be related to more destructive lesions. Gadolinium-enhanced T_1 imaging is known to show breakdown of the blood-brain-barrier associated with acute disease activity. However, the poor correlation between MRI measures such as T_2 lesion load and clinical observations is rather disappointing.

Magnetization transfer (MT) imaging is an MRI technique that, in contrast to conventional methods, permits indirect imaging of the macromolecular component of tissue. The distinct contrast obtained is based on the exchange of magnetization that occurs between protons of water molecules and of larger molecules found in tissue. Like conventional imaging, it can be performed in a semi-quantitative manner to produce image contrast

based mostly on the observable MT effect, or quantitatively to provide direct measures of the characteristics of MT. Because it can provide information about tissue content and structure, it has the potential to fill the gaps in the information provided by conventional MRI.

When applied to multiple sclerosis, MT imaging has revealed focal changes in the exchange process in lesions, and even in normal-appearing tissue predating the appearance of lesions. MT imaging thus has potential in the study of neurological disease evolution and progression, and has already contributed to the understanding of changes that occur in MS. The most common method of MT imaging is to calculate a single, semi-quantitative parameter referred to as the magnetization transfer ratio (MTR). However, the use of this ratio is limited in the view it offers of the constituent components of the MT effect.

Quantitative MT imaging (qMTI) is a recently developed MRI technique based on a two-pool model of MT in tissue. This method provides measures of parameters that describe the process of magnetization exchange. It is believed that qMTI will provide a better understanding of MT in normal tissue, as well as of the changes that occur in MS. In particular, it may help overcome the confounds resulting from the pooling of the entire MT effect into a simple MTR.

This thesis explored these possibilities via a cross-sectional study of a group of MS patients and healthy age-matched controls. The methods and results of this study are presented. Background information on the topics of MRI and multiple sclerosis is presented in Chapter 2. Chapter 3 then provides an in-depth look at magnetization transfer imaging, as well as the model for quantitative imaging. The experimental methods, including imaging protocol, parameter estimation, and extraction of results, are outlined in Chapter 4. The re-

sults are presented and analyzed in Chapter 5, and finally, these are discussed in Chapter 6. The conclusion in Chapter 7 summarizes the work done and closes by proposing avenues for future work.

Chapter 2

Background

2.1 Basics of Magnetic Resonance Imaging

The discovery of nuclear magnetic resonance (NMR) by Purcell [1] and Bloch [2] earned them the Nobel prize for physics in 1952. The discovery set off a trail of experiments throughout the latter half of the 20th century probing the properties of various nuclei via their interaction with applied magnetic fields. In 1973, Lauterbur described the use of gradients in the applied magnetic field to spatially encode the NMR signal, making NMR imaging (NMRI) possible [3]. Damadian and collaborators made use of NMR to detect cancerous tumours [4], and completed construction of the first full-body NMR imaging scanner in 1977. This section presents a brief review of magnetic resonance imaging (MRI) concepts, based on the more complete descriptions offered by Haacke *et al.* [5], and Nishimura [6].

Nuclear Magnetic Resonance

A thorough description of NMR requires quantum mechanics; however, classical concepts are sufficient to paint a clear picture of the basics of MRI. Nuclei with odd numbers of protons and/or neutrons (*odd* nuclei) demonstrate spin angular momentum, or simply, *spin*. The most common nucleic species used in MRI is the hydrogen proton (^{1}H); sodium (^{23}Na) and phosphorus (^{31}P) are other possibilities.

Spin angular momentum is a vector quantity directly related to the spin operator of quantum mechanics:

$$\mathbf{S} = \hbar \mathbf{I}, \tag{2.1}$$

where $\hbar = h/2\pi$, and h is Planck's constant. The nucleus' magnetic dipole moment μ is then related to spin angular momentum via the gyromagnetic ratio γ:

$$\boldsymbol{\mu} = \gamma \mathbf{S}. \tag{2.2}$$

The gyromagnetic ratio γ varies according to the nucleic species. For hydrogen protons, $\gamma/2\pi = 42.58$ MHz/Tesla.

Under normal circumstances – no applied external magnetic field – the orientation of the magnetic moments in a given sample is random. However, when placed in an external magnetic field $\mathbf{B}$, the nuclear spins will tend to align either parallel (n_+) or anti-parallel (n_-) to the field, the low- and high-energy states respectively. The energy difference between the two states is given by Equation 2.3.

$$\Delta E = h\frac{\gamma}{2\pi}B \tag{2.3}$$

Thermal energy is enough to ensure that the high-energy state will also be occupied, and that the ratio of the two populations will depend on the Boltzmann distribution:

$$\frac{n_-}{n_+} = \mathrm{e}^{-\Delta E/kT}, \tag{2.4}$$

where k is Boltzmann's constant and T is the temperature. A slight excess of spins will occupy the lower-energy parallel state, typically a few parts-per-million. This excess results in the net nuclear magnetization $\mathbf{M}$ of the sample.

In the classical view, a spin placed in an external magnetic field, oriented at an angle to this field, will experience a net torque $\boldsymbol{\tau}$ equal to the rate of change of spin angular momentum:

$$\boldsymbol{\tau} = \frac{d\mathbf{S}}{dt} = \boldsymbol{\mu} \times \mathbf{B}, \tag{2.5}$$

or,

$$\frac{d\boldsymbol{\mu}}{dt} = \boldsymbol{\mu} \times \gamma\mathbf{B}, \tag{2.6}$$

Summation over the entire sample, $\mathbf{M} = \sum\boldsymbol{\mu}$, yields an equation for the magnetization vector:

$$\frac{d\mathbf{M}}{dt} = \mathbf{M} \times \gamma\mathbf{B}, \tag{2.7}$$

The solution to this equation is for the spins to precess about the axis of the applied field. The precession frequency is called the Larmor or *resonance* frequency, and is given by the Larmor equation (2.8).

$$\omega_0 = \gamma B_0. \tag{2.8}$$

Thus, the constant γ also relates the resonance frequency to the magnetic field strength. The resonant frequency of hydrogen in a typical MRI scanner is in the radio-frequency (RF) range (e.g. roughly 63 MHz, at 1.5 T).

Excitation

Once resonance is established by placing the sample in a magnetic field, supplied by the scanner's main magnet, application of a second magnetic field $\mathbf{B}_1(t)$, of much lesser amplitude, may be used to probe it. The applied field will tip the magnetization away from its longitudinal alignment and cause it to nutate at the resonance frequency, as in Figure 2.1.

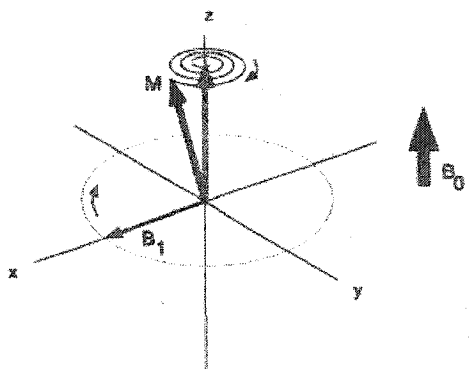

Figure 2.1: Schematic illustration of the nutation of the magnetization vector M when the field $\mathbf{B}_1$ is applied at frequency ω_0 (from [6]).

This field is optimally a combination of two orthogonal and linearly polarized magnetic fields, combining to form a circularly polarized, or quadrature, field:

$$\mathbf{B}_1 = B_1 \left[\hat{\mathbf{x}} cos(\omega t) - \hat{\mathbf{y}} sin(\omega t)\right]. \tag{2.9}$$

Optimal energy absorption occurs when the $\mathbf{B}_1$ field is tuned to the RF resonance (i.e.. $\omega = \omega_0$). When this tuned RF field is applied to the net magnetization, it has the effect of rotating it away from the longitudinal axis (z, parallel to the main magnetic field's axis), and into the transverse plane (x-y, perpendicular to the main field's orientation), as illustrated in Figure 2.2. The resultant flip angle depends on the strength B_1 and duration τ of the applied field:

$$\Delta\theta = \gamma B_1 \tau. \tag{2.10}$$

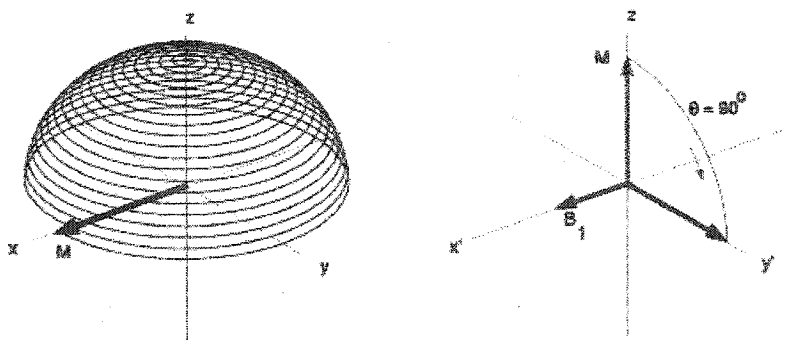

Figure 2.2: Schematic illustration of the effect of RF excitation on magnetization M in a stationary frame of reference (*left*) and in a frame of reference rotating at a frequency ω_0 (*right*) (from [6]).

The B_1 field is normally applied in the form of pulses of finite duration, known as *RF pulses*. *Off-resonance* pulses, which are used extensively in this thesis, are pulses applied at a frequency other than that of resonance ($\omega \neq \omega_0$).

Relaxation

When the RF field is turned off, the magnetization returns to its initial longitudinal state, in a process called relaxation. The first relaxation mechanism is the recovery of longitudinal magnetization, termed *spin-lattice* relaxation. It is due to interaction between the spins and their atomic environment. This recovery is described by Equation 2.11, where the rate of recovery is proportional to the difference between the magnetization $M_z(t)$ and its steady-state value M_0.

$$\frac{dM_z}{dt} = \frac{M_0 - M_z(t)}{T_1} \tag{2.11}$$

It has the following solution:

$$M_z(t) = M_z(t_0)e^{-\frac{t-t_0}{T_1}} + M_0(1 - e^{-\frac{t-t_0}{T_1}}), \tag{2.12}$$

given the arbitrary initial component $M_z(t_0)$, after excitation. T_1, the spin-lattice relaxation constant depends on field strength, as seen in Figure 2.3. The inverse of T_1, denoted by R_1, is referred to as the relaxation constant or relaxivity.

The second relaxation mechanism results from *spin-spin* interaction, and acts on the transverse component of magnetization M_{xy}. Intuitively, transverse magnetization should decay at the same rate as the recovery of longitudinal magnetization. However, interaction

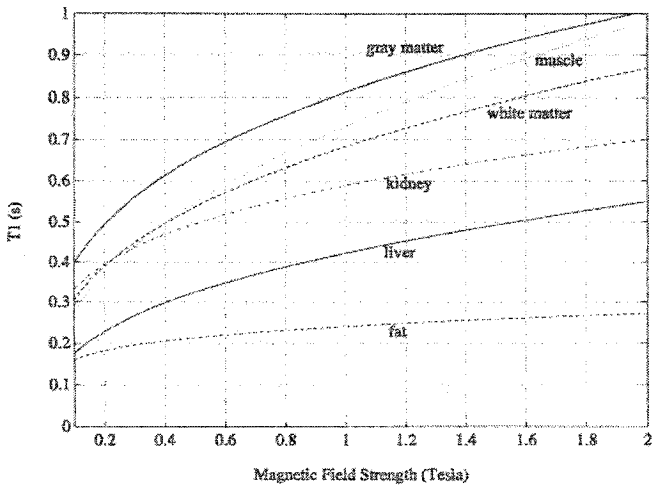

Figure 2.3: Approximate T_1 values in selected human tissue as a function of magnetic field strength B_0 (from [6]).

between spins has a dramatic effect on transverse signal decay via spin dispersion. This dephasing of spins results in a large reduction in relaxation time, so that transverse magnetization decays away more quickly than longitudinal magnetization can recover. Decay of transverse magnetization is described by the simple differential equation:

$$\frac{dM_{xy}}{dt} = -\frac{M_{xy}(t)}{T_2}, \tag{2.13}$$

and solution:

$$M_{xy}(t) = M_{xy}(t_0)e^{-\frac{t}{T_2}}, \tag{2.14}$$

The *spin-spin* relaxation time constant T_2 is smaller than T_1, on the order of tens to hundreds of milliseconds for most biological tissue. Typical values of relaxation times for selected tissues, at 1.5 Tesla, are given in Table 2.1.

Table 2.1: Typical values of T_1 and T_2 for biological tissue (from [5]).

Tissue	T_1 (ms)	T_2 (ms)
gray matter	950	100
white matter	600	80
muscle	900	50
cerebro-spinal fluid	4500	2200
fat	250	60
blood	1200	100-200

Additional decay of the transverse magnetization results from external field inhomogeneities, resulting in a shorter observed decay time constant, T_2^*, that includes the additional term T_2':

$$\frac{1}{T_2^*} = \frac{1}{T_2} + \frac{1}{T_2'}. \tag{2.15}$$

This additional decay is recoverable by making use of additional RF pulses to refocus M_{xy} to produce a "spin echo" that is dependent on T_2 only.

The Bloch Equation

If we collect the terms for precession (Eq. 2.7) and relaxation (Eqs. 2.11 and 2.13), we obtain an equation that describes the dynamics of NMR behaviour, known as the Bloch equation,

$$\frac{d\mathbf{M}}{dt} = \mathbf{M} \times \gamma\mathbf{B} - \frac{M_x\hat{\mathbf{x}} + M_y\hat{\mathbf{y}}}{T_2} - \frac{M_z - M_0}{T_1}\hat{\mathbf{z}}. \tag{2.16}$$

Signal Detection

Detection of NMR signal is made possible by Faraday's law of induction, which states that a time-varying magnetic flux ϕ_m will induce an electromotive force (*emf*) in a conducting loop:

$$emf = -\frac{d\phi_m}{dt}. \tag{2.17}$$

Each nuclear spin produces its own minute magnetic field. Given the number of spins present in any part of the human body, the collective magnetic field is enough to produce a detectable flux. The ensemble of precessing spins produces a varying flux which induces an *emf* in the receiver coil (which may or may not be the same as the transmit coil), and so an NMR signal is detected. The signal is then demodulated and filtered to remove the carrier frequency component (on resonance), leaving the modulations imparted by the gradients and the NMR properties of the subject. The basic NMR signal is called a *free induction decay*. Its carrier frequency is the resonance frequency, and its amplitude decays with the relaxation time T_2^*.

Imaging

After nuclear spin resonance and excitation, the final requirement of MRI is the magnetic field gradient. Magnetic field gradients are linear variations additional to the main magnetic field experienced by the sample. These can be turned on and off, and are produced using 3 sets of orthogonal coils, which can be combined to provide magnetic field gradients in any direction. Their effect is to locally modify the precession frequency of spins.

Gradients can be used to make RF excitation *slice-selective*, when combined with shaped pulses that excite only a range of frequencies. These are also used to encode the phase of spins prior to signal readout as well as their precession frequency during readout, providing an elegant means of signal localization. Finally, gradients are also used to produce echoes (the *gradient-recalled echo*), as we will see below.

In deriving a solution to the basic Bloch equation, we need only consider transverse magnetization $M_{xy}(t)$, as longitudinal magnetization is never detected directly. A convenient description of M_{xy} uses the complex notation $\exp(-i\omega t)$, and so we define:

$$M_{xy} = M_x + iM_y, \tag{2.18}$$

$$M_{xy,0} = M_{x,0} + iM_{y,0} \tag{2.19}$$

Considering generalized time-varying and non-uniform fields, where variations can be caused by off-resonance effects as well as gradients,

$$\mathbf{B}(\mathbf{r},t) = [B_0 + \Delta B(\mathbf{r},t)]\,\hat{\mathbf{z}}, \tag{2.20}$$

the generalized Bloch equation for the transverse component takes the following form:

$$\frac{dM_{xy}}{dt} = -\left(\frac{1}{T_2(\mathbf{r})} + i\left[\omega_0 + \Delta\omega(\mathbf{r},t)\right]\right) M_{xy}, \tag{2.21}$$

where $\omega_0 = \gamma B_0$ and $\Delta\omega(\mathbf{r},t) = \gamma \Delta B(\mathbf{r},t)$. The general solution to this equation is:

$$M_{xy}(\mathbf{r},t) = M_{xy,0}(\mathbf{r})\, e^{-t/T_2(\mathbf{r})} e^{-i\omega_0 t} \exp\left(-\int_0^t \Delta\omega(\mathbf{r},\tau)\, d\tau\right), \tag{2.22}$$

In the case where the field is composed of the static main field and time-varying gradients, we have that $\Delta\omega(\mathbf{r},t) = \gamma\mathbf{G}(t)\cdot\mathbf{r}$, and

$$M_{xy}(\mathbf{r},t) = M_{xy,0}(\mathbf{r})\, e^{-t/T_2(\mathbf{r})} e^{-i\omega_0 t} \exp\left(-\gamma\int_0^t \mathbf{G}(\mathbf{r},\tau)\cdot\mathbf{r}\,d\tau\right). \tag{2.23}$$

To obtain an equation for the MRI signal $s(t)$ from a 2-D slice, we must integrate the magnetization first over the entire volume, while ignoring relaxation (justified by the fact that T_2^* decay is negligible over the sampling interval). We may also drop the term $\exp(-i\omega_0 t)$, which is eliminated when the signal's baseband component is filtered out. If we define $m(x,y)$ as the magnetization found in the slice (integrated over the slice direction, z), the MRI signal has the form:

$$s(t) = \int_{-\infty}^{\infty}\int_{-\infty}^{\infty} m(x,y)\exp\left(-i\gamma\int_0^t \mathbf{G}(\tau)\cdot\mathbf{r}\,d\tau\right)dxdy. \tag{2.24}$$

Furthermore, we need only consider x and y gradients since 2-D signal localization is required. If we define $k_x(t)$ and $k_y(t)$ from the integrals of the gradient waveforms of their duration (during phase encoding and readout) as in equation 2.25.

$$\begin{aligned} k_x(t) &= \frac{\gamma}{2\pi}\int_0^t G_x(\tau)d\tau \\ k_y(t) &= \frac{\gamma}{2\pi}\int_0^t G_y(\tau)d\tau \end{aligned} \tag{2.25}$$

The final signal equation is then reduced to

$$s(t) = \int_{-\infty}^{\infty}\int_{-\infty}^{\infty} m(x,y)e^{-2\pi i[k_x(t)x + k_y(t)y]}dxdy. \tag{2.26}$$

Looking at Equation 2.26, a direct parallel can be drawn with the Fourier transform. Joseph Fourier, a French mathematician, developed a transform which permits representation of any function by its frequency content, in *k-space*. The 2-D form and its inverse are written as:

$$F(k_x, k_y) = \frac{1}{\sqrt{2\pi}} \int_{-\infty}^{\infty} \int_{-\infty}^{\infty} f(x, y) e^{-2\pi i (k_x x + k_y y)} dx dy \tag{2.27}$$

$$f(x, y) = \frac{1}{\sqrt{2\pi}} \int_{-\infty}^{\infty} \int_{-\infty}^{\infty} F(k_x, k_y) e^{2\pi i (k_x x + k_y y)} dk_x dk_y. \tag{2.28}$$

Consequently, image reconstruction is made relatively straightforward by making use of the Fourier interpretation of MRI. The MRI signal $s(t)$ is acquired directly in k-space, and the image is reconstructed using an inverse Fourier transform. In practice, data is discretely sampled and a fast-Fourier transform (*FFT*) algorithm is normally used.

MRI Experiments

An MRI experiment consists of probing the sample using a set of RF and gradient pulses – the pulse sequence – repeated in order to acquire the k-space data for the entire image in separate parts. A protocol is an instance of a pulse sequence with a given set of parameters. Important sequence parameters are listed below.

repetition time (TR) time period of sequence repetition

echo time (TE) time between excitation and echo formation

flip angle of the excitation pulse (α) angle to which longitudinal magnetization is rotated to create transverse magnetization (signal)

gradient characteristics direction, duration, amplitude, and slew rate

field of view (FOV) and image resolution determined by the separation of k-space samples, and by the extent of k-space covered (controlled via gradients)

other parameters characteristics of other RF pulses (such as refocusing or saturation pulses), inversion time (in the presence of inversion pulses)

Signal readout is normally set so that the origin of k-space is acquired at time TE, when the echo occurs, in order to maximize the average signal of the image.

The most basic of the imaging sequences is the *gradient echo*, where a single excitation pulse is used and gradients are played out to create an echo that is T_2^* dependent in amplitude (by reversing direction in k-space during readout). The *spin echo* sequence makes use of a second RF pulse to refocus the dephasing spins and create a spin-echo that is T_2 dependent. *Inversion recovery* sequences have an initial inversion (180°) pulse followed, after some time TI, by excitation and readout. Turbo spin-echo and echo-planar sequences acquire multiple lines of k-space per repetition for faster imaging, at a cost in signal-to-noise ratio (SNR).

Finally, contrast between biological tissues is produced in MRI by exploiting the differences in their NMR properties. Conventionally, differences in relaxation times (T_1, T_2) and proton density (PD) of tissue are used to provide contrast. By setting the repetition and echo times accordingly, contrast can be controlled. A TR on the order of shorter tissue T_1's will introduce more T_1 weighting, separating the longer components from the shorter ones according to their different amounts of recovery between repetitions. A TE on the order of tissue T_2's will introduce a distinction between tissues with short and long T_2, while much

shorter values of TE will eliminate this T_2 weighting. A scan with little T_1 or T_2 weighting is said to be proton density (PD) weighted.

Saturation and inversion pulses may also be used for specific tissue attenuation. Other properties of tissue such as molecular diffusion and magnetization exchange may also be exploited to produce contrast, as we will review in Section 2.3.

2.2 Multiple Sclerosis

Multiple sclerosis (MS) is an autoimmune inflammatory disorder of the central nervous system (CNS). It was first described by Charcot in 1868 [7]. Between 1 and 2.5 million individuals are now affected worldwide, with the highest prevalence in northern Europe, North America, and southern Australia. Onset usually takes place in early adulthood, and women outnumber men two-to-one in those affected. With a lifetime risk of 1 in 400, it is considered to be the most common cause of neurological disability in young adults [8, 9].

MS mostly affects white matter, causing physical disability as well as cognitive and sensory impairment in those affected. In 80 percent of cases, the clinical course is relapsing-remitting (RR-MS). This course is characterized by an alternating succession of acutely symptomatic periods – referred to as attacks or exacerbations – and fully or partially asymptomatic remission periods. Common symptoms include paralysis, sensory disturbances, lack of coordination and visual impairment [10]. Lasting disability may linger beyond attacks. In roughly 70 percent of RR-MS individuals, disease progression will enter a secondary progressive (SP-MS) phase after 5-10 years. During the SP phase, gradual decline of patients' condition replaces the alternating attack-recovery pattern.

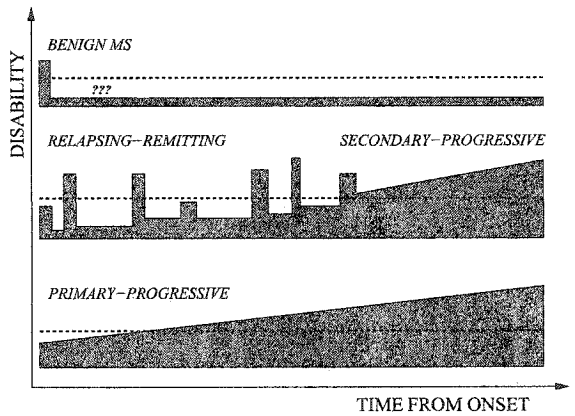

Figure 2.4: Illustration of the progression of MS types: benign, relapsing-remitting, secondary-progressive, and primary-progressive. Dashed line illustrates threshold for observation of clinical disability symptoms.

The remaining 20 percent of MS cases present either with a progressive course from onset, described as primary-progressive (PP-MS); or, without relapses and lasting disability, a course known as benign MS. These patients usually do not present with acute exacerbations. The progression of PP-MS and SP-MS patients are similar [9]. Figure 2.4 plots disability versus time, illustrating how MS develops in various disease courses. The dashed line indicates the threshold for clinical observation of symptoms and disability.

The cause of MS is unknown: genetics as well as environment are both possible factors [9]. At the pathological level, many factors contribute to the evolution of MS, and its disabling effects on those affected. Myelin loss, axonal injury, neuronal degeneration, spinal cord lesions, and brain atrophy all play a role in disease progression.

The formation of lesions in the white matter (WM) of the central nervous system is due to engagement of the immune system against the myelin sheath protecting the axons of neurons. Breakdown of the blood-brain barrier allows lymphocytes to reach and attack this protective sheath, causing acute inflammation and loss of myelin. Destruction

of myelin translates into a loss of efficiency in axonal conduction, and exposure of axons. Certain regions tend to be more affected, such as the periventricular WM. Re-myelination is known to occur in some cases, especially early in the disease: this may partly explain the relapsing-remitting nature of some MS [9]. However, demyelination is often accompanied by axonal injury, and eventual formation of chronic sclerotic plaques with progression of the disease [8].

Although much is known about the importance and the mechanisms of demyelination in MS, correlation with clinical observations remains elusive. Myelin breakdown has been observed in the normal-appearing white matter (NAWM, white matter showing no visible lesions on MRI) of patients [11], hinting at CNS-wide involvement of the disease. Lesion heterogeneity may also explain the wide range of clinical observations [12].

Observed by Charcot from the beginning, axonal injury has recently become more prevalent in the understanding of MS. Lesion aging normally demonstrates progressive loss of axons. Interestingly, several studies have observed axonal loss not only in lesions, but also in the NAWM of patients, possibly a result of Wallerian degeneration. Now suggested to occur independently of myelin loss, axonal injury may be more closely tied to clinical disability [13].

While study of white matter demyelination and axonal loss remains at the forefront of research into MS, other aspects are being explored as well. Gross brain atrophy seems to correlate well with gradual disease progression [11], while spinal cord injury and atrophy is strongly tied to disability [10]. Most recently, cortical lesions have been proposed as an additional characteristic of MS [14]. More detailed views of MS pathology are offered by Hemmer *et al.* [15], Wingerchuk *et al.* [16], and Smith and McDonald [17].

Diagnosis of MS remains largely clinical, though MRI now plays a more important role. Diagnostic procedures were initially standardized by the Poser committee [18], and were more recently revised by MacDonald *et al.* [19], and now include MRI. Diagnosis requires two clinical relapses, and is normally confirmed by at least a pair of lesions disseminated in both time and space. Clinical status is often evaluated using Kurtzke's expanded disability status scale (EDSS) [20], on a scale of 0-10, with 0 representing normal function and 10 death.

The prognosis for patients affected by MS varies greatly: the course of the disease is largely unpredictable. Life expectancy is generally at least 25, and up to 50, years from onset, with most patients dying from unrelated causes. In roughly one quarter of cases, MS will not greatly affect daily activities of the patient; conversely, up to 15 percent become severely disabled within a short time. While there is no cure, treatment options have come a long way in the past decade, helping patients cope with the disease. Treatment aims at reducing relapse rates, managing symptom, preventing relapse-caused and progressive long-term disability, and treating established progression [8]. Further insights into the diagnosis, disease course, and prognosis of MS, are provided by Keegan and Noseworthy [21].

Magnetic resonance imaging has provided very useful insight into MS, and constitutes a powerful means of studying the disease *in-vivo*. We explore the impact of MRI on the disease in the next section.

2.3 MRI of Multiple Sclerosis

In the past 15 years, magnetic resonance imaging has had an important role to play in the diagnosis and study of multiple sclerosis. MRI of the central nervous system is now established as the most sensitive and most important para-clinical tool in diagnosis and monitoring of the disease. This section presents a brief review of MRI methods used in the study of MS. Further reviews have been published outlining the role of MRI in MS [22], and in particular for disease diagnosis [23] and monitoring [24].

The involvement of MRI in the study of MS spans use as a diagnostic tool or in the study the natural progression of the disease, monitoring, and prognostic functions: imaging is used routinely in both clinical and research settings. Conventional MRI measures have shown that the cerebrum is almost always involved, and the spinal cord is also frequently affected [8]. Although the presence of white matter abnormalities on T_2-weighted scans is not sufficient for diagnosis of MS, these are present in more than 95% of patients. The disease is also considerably more active on MRI: lesion occurrence is seven to ten times more frequent than clinical relapses [21, 17].

Conventional techniques, such as T_2, T_1, and proton density weighted imaging, have helped further the understanding of the pathophysiology of MS. Contrast agent imaging using Gd-DTPA, a compound of the paramagnetic element gadolinium, enables the observation of blood-brain barrier breakdown. More recent advancements in magnetization transfer imaging (MTI), diffusion imaging, and proton magnetic resonance spectroscopy imaging (^{1}H-MRSI) are now providing further insight into the progression of the disease, in particular with regards to the involvement of so-called silent areas (showing no lesions).

MRI for Diagnosis and Prognosis

MRI has attained an important role in the diagnosis of MS: while still largely clinical, the approach to diagnosing MS is making increasing use of MRI. In addition to the standardized clinical protocol of Poser *et al.* [18], MRI evidence can now legitimately support clinical findings in the diagnostic process [25, 19].

Evaluation of the risk for progress in MS patients is another important focus, as it may impact the type of treatment prescribed. Mono-symptomatic patients who present with two or more cerebral MRI lesions are at far great risk ($> 85\%$) of relapsing within the following ten years than patients with one or no brain lesions [26]. For this reason, MRI monitoring of MS patients has become common practice, as well as the use of MRI in trials to evaluate the efficacy of drug treatments.

Conventional Methods

The combination of T_2 and proton density (PD) weighted MRI is the standard technique for detection and monitoring of focal white matter abnormalities. The two are most often acquired as part of the same high-resolution spin-echo sequence: two acquisitions at different echo times (TE) provide the distinct contrast weightings. Lesions appear hyperintense on both types of scan, as seen in Figure 2.5.

Increases in T_2 reflect increases in water content: T_2-weighted imaging can thus be conceived to reflect edema and tissue destruction early in lesion development, and demyelination and gliosis in later stages [25]. PD-weighted imaging provides intermediate weighting between T_2 and T_1, aiding in the distinction of periventricular lesions from cerebro-spinal

fluid (CSF). T_2- and PD-weigthed scans are highly sensitive in detecting lesions but offer little specificity in differentiating among them.

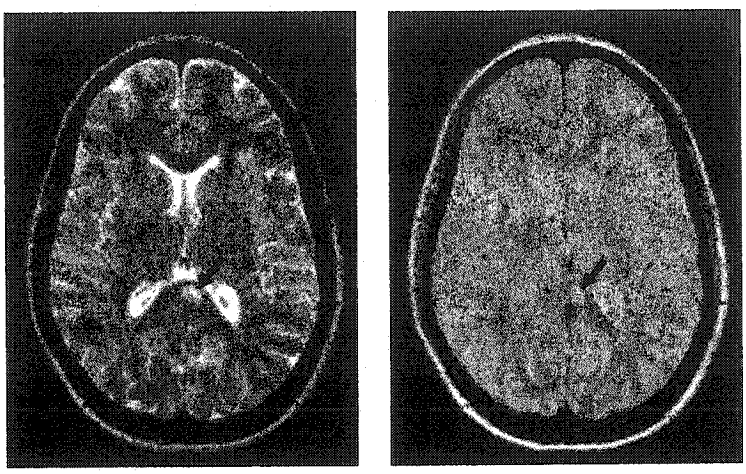

T_2 PD

Figure 2.5: Example T_2 and PD-weighted images of an MS patient, showing a lesion in the splenium of the corpus callosum.

Several techniques lend themselves to T_2/PD imaging. Conventional spin-echo (CSE) is an established, robust, yet relatively slow, sequence; faster techniques that acquire multiple lines of k-space per repetition, such as fast spin echo (FSE) and turbo gradient spin echo (TGSE), are steadily replacing CSE [22]. Although it continues to be investigated, the correlation between T_2/PD-weighted lesion burden and clinical status in MS patients is poor [27]. Lack of correlation between T_2/PD-weighted lesion burden and locomotor and cognitive dysfunction is most likely related to the poor pathological specificity of such hypointensities [22].

T_1-weighted imaging of MS demonstrates focal hypointensities, but these are often smaller in size and less numerous than T_2-weighted hyperintensities. An example of such a lesion is seen in Figure 2.6. These T_1 "black holes" are associated with acute edema or tissue destruction: chronic hypointensities are also more specific than T_2 hyperintensities in pinpointing destructive pathology [25, 28]. Histological studies have shown chronic T_1 lesion weighting to correlate with myelin breakdown and axon loss [28], while imaging studies have shown correlations of T_1 weighting with lower magnetization transfer ratios (see subsection on MT imaging), linked to myelin breakdown [29, 30]. T_1-weighted imaging is performed using conventional techniques (*i.e.* CSE, TGSE), with TR and TE adjusted accordingly.

Gadolinium is the paramagnetic contrast agent most commonly used in MRI, usually incorporated into diethyltriaminepentaacetic acid (DTPA) to form the labeled compound Gd-DTPA. When injected prior to a T_1-weighted scan, Gd-DTPA will introduce hyperintensities wherever it is present in the image.

Persisting from two to six weeks from lesion onset, Gd-enhancement marks the inflammation and opening of the blood-brain barrier (BBB) characteristic of lesion initiation, thus increasing the sensitivity of these scans to MS plaques. Conversely, it provides little information about the extent or severity of this inflammatory phase [24, 25]. Single and triple dose (0.1 mmol/kg and 0.3 mmol/kg, respectively) studies have been performed to study the differences in the number of detectable lesions [31, 32], as well as the influence of the time delay between injection and imaging.

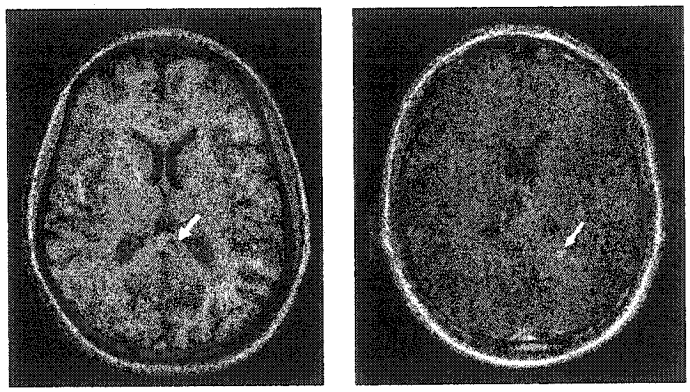

T_1 Gd-enhanced

Figure 2.6: Example T_1-weighted image of an MS patient, showing a lesion in the splenium of the corpus callosum (*left*); example scan of an MS patient with a Gd-enhancing lesion (*right*).

New Methods

New MRI measurements have emerged over the past decade that have contributed greatly to the understanding of MS. They include relaxometry, diffusion imaging, proton magnetic resonance spectroscopy imaging (^{1}H-MRSI), magnetization transfer imaging (MTI), as well as functional magnetic resonance imaging and quantitative analysis techniques. The greater pathological specificity afforded by these techniques has enabled researchers to differentiate inflammation from tissue destruction, and to study pre-lesional and whole-brain characteristics of normal-appearing tissue.

Relaxometry

Relaxometry is the quantitative measurement method by which one can obtain maps of relaxation time constants, rather than simple qualitative weighting. Although techniques for T_1 and T_2 relaxometry are different, the concept remains the same for both cases. One must

sample the relaxation curve of the components of magnetization (longitudinal recovery in the case of T_1, transverse decay in the case of T_2) over a satisfactory time interval to enable robust exponential fitting.

In the case of T_1, saturation or inversion recovery techniques are most often used: variations in inversion and/or echo times permit sampling of the recovery curve. Fast (or single-shot) techniques have also been developed [33]. T_2 relaxometry measurements are usually performed using multi-echo spin-echo sequences with anywhere from 2 to 64 echoes [34]. Due to the importance of relaxometry within the protocol used in this work, the techniques used will be described in greater detail in the next chapter.

In MS, it is known that tissue NMR relaxation times change considerably. Lesions demonstrate significantly longer T_1 [35] and T_2 [36], due to increased water content and tissue matrix breakdown. Pre-lesional tissue and normal-appearing tissue tend to exhibit some change, however slight. Relaxometry is able to measure these changes, and with improving technique, should be able to provide site-to-site comparisons due to its potential hardware and sequence independence. However, truly robust and consistent techniques remain to be developed.

NMR relaxation in brain tissue has repeatedly been shown to be mono-exponential along the longitudinal axis; however, transverse decay exhibits multiple components depending on the complexity of the environment in which the protons are located. Multi-component T_2 measurements have been proposed and implemented as a method of tissue characterization [37]. The acquisition is identical to standard T_2 relaxometry, with the exception that a sufficient number of echoes must be collected (e.g. 32) to allow differentiation of the components.

Menon [38] initially observed *in vitro* normal white matter to exhibit four main T_2 components. MacKay *et al.* [39] observed 3 of those components *in vivo*: a short (15-30 ms) component, believed to be associated with water compartmentalized within the myelin bilayer; an important medium component (70-100 ms), linked to intra- and extra-cellular water; and a long component (about 2 s) tied to the presence of CSF. Signal from the fourth component decays away too quickly to be observed directly in MRI, and is attributed to the hydrogen nuclei present in macromolecules.

Multi-component T_2 analysis has been used to produced so-called myelin maps [40]. More importantly, significant decreases in myelin water content have been observed in MS [39], leading to the belief that demyelination could be directly measured using multi-component T_2 analysis.

Diffusion Imaging

Diffusion imaging is a technique that produces contrast based on the random movement of water molecules within tissue [41]. The method typically employs pairs of strong magnetic field gradients placed symmetrically about a 180° pulse. These gradients have the effect of dephasing and rephasing the static water protons, while leaving diffusing water protons dephased, thus creating diffusion-dependent signal attenuation.

One can obtain measures of both the magnitude of the apparent diffusion coefficient (ADC), and the anisotropy index (via the shape of the diffusion displacement profile). The diffusion coefficient reflects water content, and the presence of restricting barriers due to tissue structure and organization. The anisotropy index depends mostly on the structure of restricting barriers.

In MS, changes have been observed in both parameters. The ADC has been observed to increase in lesions and NAWM, reflecting increasing water content and tissue breakdown [42]. Breakdown of tissue barrier structures is confirmed by the decrease observed in anisotropy [43].

Proton Magnetic Resonance Spectroscopy

Proton magnetic resonance spectroscopy imaging (^{1}H-MRSI or simply MRSI) makes use of the chemical shift observed in the MR signal of certain species found in tissue to study changes in the CNS [44]. This method records the off-resonance signal from metabolites such as N-acetylaspartate (NAA), creatine (Cr), and choline (Cho). Measurement techniques often use long echo times (100-300 ms) combined with suppression of the main water peak signal. It is a time-consuming, low SNR method yielding large voxels, but it provides information not obtainable by any other MRI technique. Relative measurements of NAA:Cr and Cho:Cr ratios are most often performed, though fully quantitative measurement can be done at a greater expense in time.

NAA, found only in mature brains, has been shown to be a marker of axonal integrity, which can be used to study the progression of MS [45]. Significant decreases in both lesion and normal-appearing white matter (NAWM) NAA points to axonal damage and loss, not only in destructive plaques but also in areas free of lesions. This loss of axonal integrity has been shown to correlate with disability [46], and more strongly than other MRI measures. NAA also correlates with the degree of ataxia observed on Kurtzke's EDSS [47].

Other Techniques

Other MRI methods have been applied successfully to the study of MS. Fluid attenuated inversion recovery (FLAIR) sequences combine an inversion pulse with long inversion time (TI) and a long echo-time (TE). This produces essentially T_2-weighted images, with the notable exception of CSF being nulled: this provides better lesion contrast than T_2/PD-weighted images, and helps differentiate lesions from CSF, particularly in the periventricular area.

Functional MRI (fMRI) records signal dependent on blood flow, volume, and oxygenation level, providing a means to study neuronal activation during specific tasks. It is extremely useful in studying motor, cognitive, and sensory brain function re-organization in patients [48, 49]. Such functional re-organization may contribute to clinical recovery from exacerbations in the RR phase of the disorder.

Spinal cord imaging often reveals lesions in MS patients. Their presence makes diagnosis more specific because spinal cord plaques, unlike their cerebellar counterparts, are not known to occur with age. Furthermore, in many patients presenting with clinical symptoms of MS yet without brain MRI abnormalities, spinal cord imaging has often confirmed diagnosis [50]. The size and shape of the spinal cord renders imaging difficult and time-consuming, as well as complicating lesion detection [25]. However, advancements in phased array coils and fast imaging sequences are improving the performance of cord imaging.

High field imaging (field strength ≥ 3 Tesla) has also been used in the study of MS. In contrast to the software advancements described, this hardware modification provides ob-

vious improvement in signal-to-noise and contrast-to-noise ratio (SNR, CNR), resolution, and imaging speed, for both MRI and MRSI. This improvement comes at a price, both in the form of new technical issues and increased monetary cost.

Finally, quantitative post-acquisition analysis methods are also playing a strong role in the study of MS. The degenerative nature of MS causes loss of axonal density and volume as well as loss of myelin [51]. Brain volume and atrophy measurements are being used to quantify these changes [52], and atrophy has been shown to correlate with increasing disability [53]. Cortical grey matter thickness has also generated interest, as it shows significant decrease in MS patients [54].

Magnetization Transfer Imaging

Magnetization transfer imaging is the focus of this thesis. Water protons are the only species visible to most MRI techniques, in addition to protons found in fat. Hydrogen nuclei composing larger molecules have T_2 values much too short for standard observation (on the order of microseconds). MT imaging is a technique that enables indirect observation of this semi-solid content in tissue. A thorough review of the technical aspects of MT imaging will be given in the next chapter.

It has been shown that in white matter, MT effects are associated with the presence of myelin lipids, most importantly galactocerebroside [55], as well as cholesterol [56] and sphingomyelin. In MS, edema and changes in macromolecular structure are known to significantly change the MT properties of white matter [57]. Focal changes in MTR are also known to occur prior to lesion appearance on conventional scans [58, 59].

While the magnetization transfer ratio (MTR) remains the standard measurement, fully quantitative MT imaging methods – such as the one utilized in this thesis – are emerging. Changes in MTR reflect a combination of changes in macromolecular content, exchange, and relaxation properties: the hope is to separate these confounding factors using fully quantitative techniques.

In summary, MRI plays an important role in the diagnosis, monitoring, and study of MS. Table 2.2 recaps the important characteristics of MS when observed by MRI. As mentioned, MRI continues to be an essential tool for study of MS, and new imaging techniques are now complementing conventional methods for this purpose. The lack of pathological specificity in conventional MRI lesions remains the main challenge facing MRI research, along with the development of robust and efficient methods for diagnosis and disease monitoring in drug trials. The next chapter will deal more specifically with one such new method, quantitative magnetization transfer imaging.

Table 2.2: MRI measurement characteristics of MS (from [25]).

Technique	**Associated pathology**
T_2 weighting	
New lesions	Inflammation
Enlarging T_2 lesion	Increasing inflammation
Chronic lesions	Nonspecific
T_1 weighting	
Acute hypointense lesions ("black holes")	Edema associated with acute inflammation
Chronic hypointense lesions	Tissue destruction with demyelination and axon loss
Gadolinium-enhanced T_1-weighting	Disruption of the blood-brain barrier
Magnetization transfer	Changes in myelin (contaminated by T_1 weighting)
MRSI	
N-acetylaspartate peak	Axon integrity
Lipid peak	Demyelination
Changes in brain volume	Brain atrophy (not specified for cell type)

Chapter 3

Magnetization Transfer Imaging

Magnetization transfer imaging (MTI) is the result of actively probing the mechanism of cross-relaxation in MRI. MTI produces contrast distinct from conventional forms (T_1, T_2, PD), and makes possible the indirect observation of the macromolecular content of biological tissue. Comprehensive reviews of MTI are offered by Balaban and Ceckler [60], Santyr and Mulkern [61], and Henkelman *et al.* [62]. This chapter reviews the principles of MTI, as well as quantitative MTI.

3.1 Basics

Biological tissue comprises a multitude of different proton environments, giving rise to complex NMR behaviour. In general, protons (^{1}H) can be considered in two distinct environments. The majority of hydrogen protons are found in small, mobile molecules, mostly in water. These experience rapid rotational and translational motion, which average out mutual magnetic dipole interactions. These relatively free hydrogen protons are characterized by a narrow Larmor spectrum (peak width $\sim$ 20 Hz) and longer T_2 values ($>$ 10 ms).

Hydrogen protons are also found in "semi-solid" macromolecules, though in smaller proportion. In contrast to *free* protons, these *restricted* protons experience relatively slow rotational and translational motion. Thus, they present a broader Larmor spectrum (peak width $\sim$ tens of kHz) and much shorter T_2 values ($\sim$ few μs). MRI-observable signal originates from the liquid pool only, as its T_2 is long enough for gradients to be switched on and an image to be acquired. Macromolecular proton signal dies out too quickly ($T_{2,r} >> \text{TE}$) to permit direct imaging.

Edzes and Samulski first proposed a description of MT mechanisms [63]. Water protons can be subdivided between hydration layer water (loosely bound to macromolecules) and mobile bulk water. These two water pools interact with the semi-solid pool via a 3-step process: (*i*) magnetization is quickly transferred between bulk water and hydration water by rapid chemical exchange, (*ii*) then between the hydration water and macromolecular protons by nuclear dipole coupling, (*iii*) and finally, rapidly distributed among macromolecular protons.

The MT process is illustrated in Figure 3.1. Exchange between the two water pools is much faster than that between water and macromolecules, so MT is normally modeled using a single water pool. From the point of view of MRI, mobile and restricted protons may exchange magnetization either by rapid chemical exchange or dipole interaction, and the two processes are indiscernible.

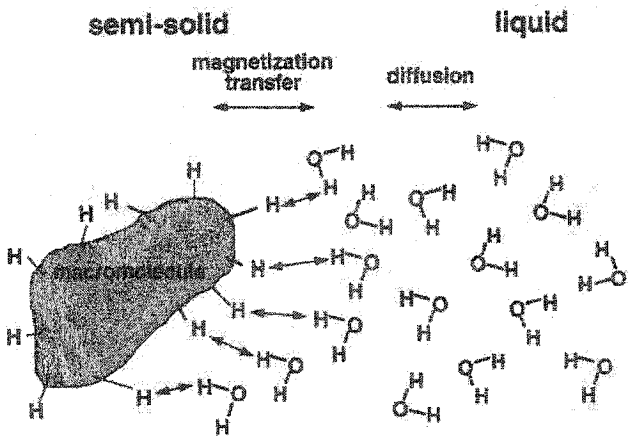

Figure 3.1: Illustration of magnetization transfer in tissue (from [64]).

3.2 Saturation Transfer and MT Contrast

Application of the saturation transfer method to MRI results in the production of magnetization transfer contrast (MTC) [65]. The method selectively saturates the semi-solid pool before image acquisition, or in an interleaved fashion as part of the pulse sequence. Saturation of the semi-solid pool creates a sink for the liquid pool magnetization (via the MT effect), producing signal attenuation in areas of significant cross-relaxation. Consequently, MTC is a unique form of MRI contrast, different from conventional forms (T_1, T_2, PD).

A saturation transfer experiment must deal with the fact that both pools have identical resonance frequencies, thus requiring a selective irradiation technique. Methods exploit the differences in T_2 values and absorption linewidth of the two pools to selectively saturate the restricted spins. To be useful in MRI, a saturation technique must be producible using standard MRI hardware, and be time-efficient. Power deposition must be efficient, to provide maximum saturation without exceeding the specific absorption rate (SAR) limits.

The original saturation transfer method was continuous wave (CW) RF irradiation [65, 66]. Long, off-resonance (5-10 kHz) RF waves of narrow bandwidth are used to prepare the magnetization prior to image acquisition. Semi-solid pool selectivity is ensured by the frequency offset, and the effective coupling between protons of the restricted pool ensures that saturation applied at a given offset frequency will spread throughout the pool. This technique is unfeasible for clinical MRI, as it is time-inefficient, leads to excessive power deposition, and is not compatible with standard MRI hardware.

Pulsed RF irradiation is now the most widely used method of selective saturation of the semi-solid magnetization component. Its increased time efficiency (via MT pulse interleaving) and lower power deposition make it suitable for use in MRI. The on-resonance variant of pulsed saturation [67] consists of brief, binomial pulses ($1\bar{1}$, $1\bar{2}1$, etc.). Free pool spins are returned to their original state by these self-compensating (0°) pulses, while restricted protons are saturated due to their faster dephasing and much shorter T_2 decay. These pulses act over the widest bandwidth, though indirect saturation of free spins is greater.

Pulsed saturation can also be applied off-resonance [68] in the form of brief, shaped, off-resonance RF pulses applied repeatedly within an imaging sequence. This results in saturation of a wider bandwidth than CW irradiation, and restricted pool selectivity is ensured again by frequency offset. This is the saturation technique employed in the present work. The effect of all three methods are illustrated in Figure 3.2.

Semi-solid pool spins are as much as 10^6 times more sensitive to appropriate off-resonance RF radiation than liquid pool spins [62]. However, complete saturation of the restricted pool is not feasible, and a small effect is observed on the liquid pool (5-15% for CW off-resonance irradiation, when effective ^1H_r saturation is achieved [60]). Off-resonance

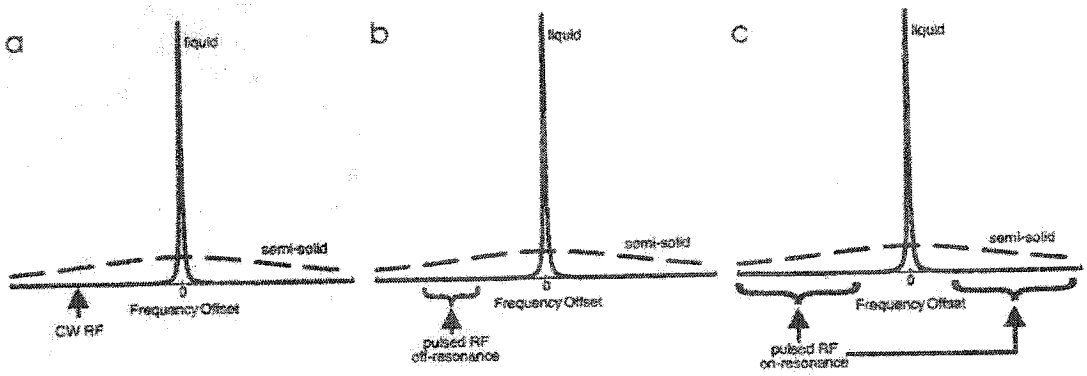

Figure 3.2: Illustration of the effect of different saturation methods (from [64]): (a) CW off-resonance, (b) pulsed off-resonance, and (c) pulsed on-resonance.

MT pulse design must consider the saturation power, the frequency of irradiation, and duration (or duty cycle) of irradiation. One may also take advantage of long restricted pool T_1 values by using short TR sequences, allowing for less saturation recovery between repetitions. The effect of off-resonance saturation pulses is described by Equation 3.1, where the saturation rate W_{sat} is equal to the product of semi-solid pool RF absorption $G(\Delta)$ at the offset frequency Δ and the average pulse power $\bar{P}_{RF}$.

$$W_{sat} = G(\Delta)\bar{P}_{RF} \tag{3.1}$$

MT saturation pulses have been added to standard acquisition sequences to produce MTC: gradient echo [66], spin-echo [69], inversion recovery [70], and spoiled gradient echo [71]. Sequences usually include gradient or RF spoiling, or phase cycling, in order to eliminate any transverse magnetization (signal) produced by the MT pulse. This ensures agreement with the simple two-pool model of saturation transfer, which assumes a steady-state condition of strictly longitudinal magnetization before the readout excitation.

Basic MTC depends on saturation pulse design as well as other sequence parameters (TR, TE, flip angle). MT saturation alone does not produce very interesting MTC images. In order to emphasize the contrast due to the MT effect, images are often acquired with and without MT pulses, and a difference image is calculated. Baseline images are normally PD or T_1-weighted scans with high SNR. To further isolate MT contrast and do away with some of the T_1 or PD weighting, one can normalize the difference image by the baseline to produce the magnetization transfer ratio, *MTR*:

$$\text{MTR} = \frac{NoSat - Sat}{NoSat} \times 100 \tag{3.2}$$

Saturation transfer has two main applications in MRI. It is widely used to enhance contrast in standard sequences, *i.e.* for angiography [72], imaging of breast, leg, knee, liver, osteoarthritis, and contrast agent imaging [73]. More importantly for this work, it can help provide information about the semi-solid pool, in semi-quantitative (MTR) and quantitative MTI (qMTI) methods. The latter yields actual measurements of model parameters. These are useful, in the present context, for the study of white matter diseases such as MS [64].

3.3 Quantitative Magnetization Transfer Imaging

Quantitative magnetization transfer imaging (qMTI) is a logical extension of MTI providing estimates of the properties of the free and restricted pools. A complete, quantitative *in vivo* technique was developed and validated by Sled and Pike [71]. Multiple MTC scans are acquired using a range of saturation parameters, as described in Chapter 4. The data is

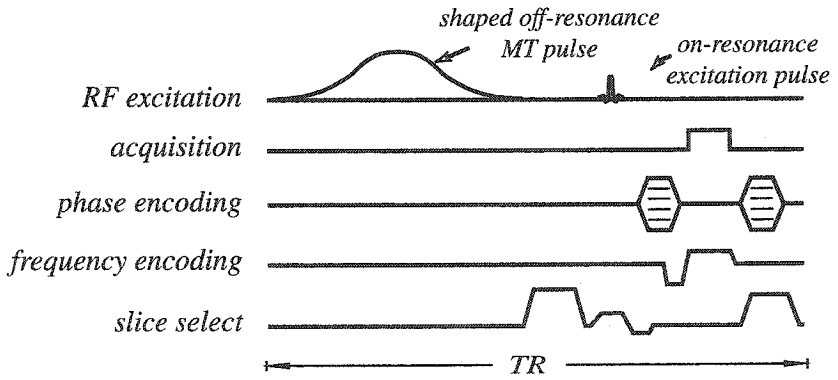

Figure 3.3: Illustration of the spoiled gradient echo pulse sequence with MT saturation (from [71]).

fitted to a model of MT in tissue, yielding parametric maps for each of the model variables.

The MT data is acquired using a spoiled gradient-echo sequence (MTSPGR), as described in detail in Chapter 4. This short TR sequence uses a non-selective shaped off-resonance MT pulse (Hanning-windowed Gaussian pulse) for saturation of the restricted pool, followed by a slice-selective small angle excitation pulse and a gradient echo readout. The sequence is illustrated in Figure 3.3.

The most commonly accepted of MT models is the binary spin bath model [74]. Exchange between bulk and hydration water is much more rapid than that between hydration water and macromolecular protons. This justifies the simplification to two distinct pools: liquid or *free* protons (^1H_f) and semi-solid or *restricted* protons (^1H_r). The model, illustrated in Figure 3.4, describes a larger liquid pool and a smaller macromolecular pool which freely exchange magnetization. The absolute pool sizes are described respectively by $M_{0,f}$ and $M_{0,r}$, and free pool magnetization is often normalized to 1. The fractional pool size ratio is defined as in Equation 3.3.

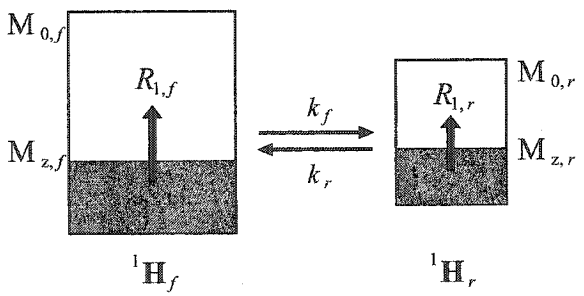

Figure 3.4: Two-pool model of magnetization transfer.

$$f = \frac{M_{0,r}}{M_{0,f}} \tag{3.3}$$

Magnetization exchange is quantified in a single rate constant R, which is in turn normalized by the pool sizes to yield the forward and reverse transfer rates:

$$k_{\text{forward}} = k_f = RM_{0,r} \tag{3.4}$$

$$k_{\text{reverse}} = k_r = RM_{0,f} \tag{3.5}$$

The relaxation time constants of each pool ($T_{1,f}$, $T_{2,f}$, $T_{1,r}$, $T_{2,r}$) complete the parameters.

Modeling the behaviour of the system requires a distinct theory for each pool. A modified version of the Bloch equation is used to describe the free pool, accounting for exchange of longitudinal magnetization with the restricted pool. The restricted pool is modeled by an equation for the inverse spin temperature, from the Redfield-Provotorov theory [75]. Experiments on agar gels confirmed that the dipolar term in the theory can be safely neglected [71]. Validation on agar also confirmed agreement with previously published data from [74].

The formulation of the model consists of the following equations, in a reference frame rotating at frequency offset Δ from resonance:

$$\frac{dM_{x,f}}{dt} = -\frac{M_{x,f}}{T_{2,f}} - \Delta M_{y,f} - \mathsf{Im}(\omega_1) M_{z,f} \tag{3.6}$$

$$\frac{dM_{y,f}}{dt} = -\frac{M_{y,f}}{T_{2,f}} + \Delta M_{x,f} + \mathsf{Re}(\omega_1) M_{z,f} \tag{3.7}$$

$$\frac{dM_{z,f}}{dt} = R_{1,f}(M_{0,f} - M_{z,f}) - k_f M_{z,f} + k_r M_{z,r} + \mathsf{Im}(\omega_1) M_{x,f} - \mathsf{Re}(\omega_1) M_{y,f} \tag{3.8}$$

$$\frac{dM_{z,r}}{dt} = R_{1,r}(M_{0,r} - M_{z,r}) - k_r M_{z,r} + k_f M_{z,f} - W M_{z,r}. \tag{3.9}$$

While the lineshape of the free pool is Lorentzian, a direct consequence of the Bloch equation, the lineshape used for the restricted pool, for biological tissue, is best described via a super-Lorentzian (Equation 3.10).

$$G(2\pi\Delta) = T_{2,r} \int_0^1 \frac{1}{|3u^2 - 1|} \exp\left(-2\left(\frac{2\pi\Delta T_{2,r}}{3u^2 - 1}\right)^2\right) du\,. \tag{3.10}$$

The saturation rate of the restricted pool during CW irradiation is:

$$W = \pi\omega_1^2 G\left(\Delta\right). \tag{3.11}$$

Equations 3.6 through 3.9 can be solved directly for the MTSPGR sequence by numerical methods, but their complexity make this time-consuming. Based on the two-pool analytic description of signal response in GRE sequences of [76], solutions to special cases of these equations were developed by Sled and Pike [77], allowing for rapid estimation from closed-form solutions. As illustrated in Figure 3.5, the MT spoiled gradient echo

sequence was decomposed into periods of free-precession, instantaneous saturation, and off-resonance CW irradiation, to approximate the effect of the set of RF pulses on each pool.

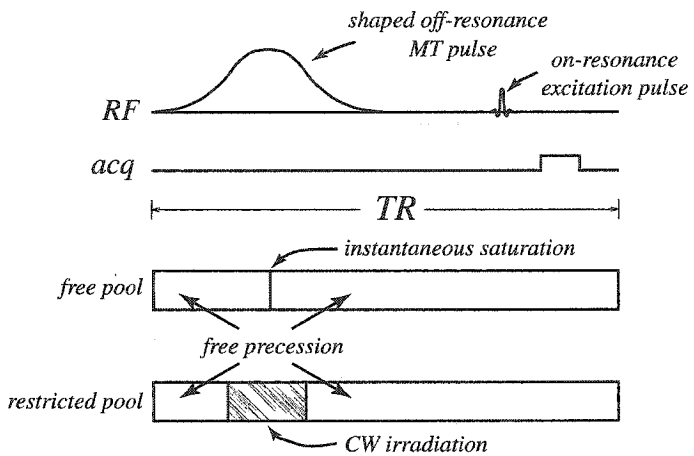

Figure 3.5: Breakdown of MT spoiled-GRE sequence into periods of free precession, on-resonance free pool saturation, and off-resonance restricted pool saturation (from [71]).

The effect of both on- and off-resonance pulses on the free pool is reduced to instantaneous fractional saturation of the longitudinal magnetization $M_{z,f}$. The fractional saturation S_f can be computed numerically by solving the Bloch equation for the free pool while ignoring exchange and T_1 recovery. On-resonance pulses are assumed to have no effect on the restricted pool, while off-resonance pulses are approximated by rectangular pulses with equivalent power and offset frequency. The sequence is thus broken down into periods of free-precession of both pools, off-resonance irradiation of the restricted pool, and instantaneous saturation of the free pool. For each of these special cases, Equations 3.6 to 3.9 are reduced to first-order equations with constant coefficients with closed-form solutions under

(periodic) steady state conditions.

A separate measurement of the apparent longitudinal recovery rate ($R_{1,obs} = 1/T_{1,obs}$) is needed, because MT measurements alone are insufficient to constrain all of the model parameters. As described in Chapter 4, this is done using a Look-Locker inversion recovery experiment. One can then determine $R_{1,f}$ ($= 1/T_{1,f}$), the longer of two apparent relaxivities, by Equation 3.12.

$$R_{1,f} = \frac{R_1^{obs}}{1 + \left(\frac{\left[\frac{k_f}{R_{1,f}} \right] (R_{1,r} - R_1^{obs})}{(R_{1,r} - R_1^{obs}) + k_f/F} \right)}. \tag{3.12}$$

The longitudinal relaxivity of the restricted pool, $R_{1,r}$, was arbitrarily chosen as 1 ± 1 s^{-1}, as the model depends only weakly on this parameter for the range of model parameters relevant to biological tissue.

Once the closed form solutions have been derived, one is left to choose the saturation parameters that best suit the experiment, and to fit the signal equation voxel-by-voxel to the experimental data to produce the tissue parameters. Corrections are applied to the results to compensate for field non-uniformities, as described in Chapter 4.

After validation of the MT model with *in vitro* experiments on uncooked beef [71] – selected for its homogeneity and super-Lorentzian lineshape – the protocol was adapted to *in vivo* imaging. The first complete sets of *in vivo* quantitative MT parametric images were produced. Model parameters were estimated for two normal controls and one RR-MS patient, and are presented in Tables 3.1 and 3.2.

As stated in Section 2.3, MTR is the established technique used in the study of cross-relaxation in tissue. However, MTR reflects a complex combination of parameters such as macromolecular content, cross-relaxation rate, and free pool longitudinal recovery rate. Our aim is to use our putative measures of these quantities provided by qMTI (f, k_f, $R_{1,f}$, along with $T_{2,f}$ and $T_{2,r}$) to separate these confounding effects in the study of lesions and normal-appearing white and grey matter in multiple sclerosis. The following chapter outlines the steps performed to complete this study.

Table 3.1: Parameter estimates for grey and white matter in from selected ROIs of two normal controls. Error estimates are for a 95% confidence interval derived from the residual error in the fit of the signal equation (from [71]).

	subject 1		subject 2	
	caudate nucleus	frontal white matter	cortical grey matter	frontal white matter
k_f	$2.2 \pm 1.0\,\mathrm{s}^{-1}$	$4.6 \pm 1.3\,\mathrm{s}^{-1}$	$2.4 \pm 0.8\,\mathrm{s}^{-1}$	$4.3 \pm 1.0\,\mathrm{s}^{-1}$
f	0.056 ± 0.010	0.152 ± 0.023	0.072 ± 0.013	0.161 ± 0.025
$R_{1,f}$	$0.99 \pm 0.16\,\mathrm{s}^{-1}$	$1.8 \pm 0.3\,\mathrm{s}^{-1}$	$0.93 \pm 0.2\,\mathrm{s}^{-1}$	$1.8 \pm 0.3\,\mathrm{s}^{-1}$
$T_{2,f}$	55 ± 8 ms	31 ± 5 ms	56 ± 8 ms	37 ± 8 ms
$T_{2,r}$	$9.7 \pm 1.6\,\mu$s	$11.8 \pm 1.3\,\mu$s	$11.1 \pm 1.3\,\mu$s	$12.3 \pm 1.6\,\mu$s
$R_{1,obs}$	$0.99 \pm 0.14\,\mathrm{s}^{-1}$	$1.72 \pm 0.25\,\mathrm{s}^{-1}$	$0.95 \pm 0.20\,\mathrm{s}^{-1}$	$1.7 \pm 0.2\,\mathrm{s}^{-1}$
$T_{2,obs}$	93 ± 5 ms	79 ± 4 ms	92 ± 3 ms	82 ± 4 ms

Table 3.2: Parameter estimates from four ROIs on a scan of an MS patient (from [71]).

	cortical grey matter	frontal white matter	lesion 1 (21+ months)	lesion 2 (1–9 months)
k_f	$2.6 \pm 1\,\mathrm{s}^{-1}$	$4.9 \pm 1.3\,\mathrm{s}^{-1}$	$2.7 \pm 0.7\,\mathrm{s}^{-1}$	$3.6 \pm 0.8\,\mathrm{s}^{-1}$
f	0.068 ± 0.011	0.15 ± 0.02	0.094 ± 0.015	0.12 ± 0.02
$R_{1,f}$	$0.89 \pm 0.1\,\mathrm{s}^{-1}$	$1.78 \pm 0.4\,\mathrm{s}^{-1}$	$1.26 \pm 0.3\,\mathrm{s}^{-1}$	$1.52 \pm 0.2\,\mathrm{s}^{-1}$
$T_{2,f}$	62 ± 11 ms	38 ± 7 ms	51.5 ± 9 ms	43 ± 6 ms
$T_{2,r}$	$9.6 \pm 1.4\,\mu$s	$11.4 \pm 1.4\,\mu$s	$10.9 \pm 1.4\,\mu$s	$10.3 \pm 1.1\,\mu$s
$R_{1,obs}$	$1.67 \pm 0.34\,\mathrm{s}^{-1}$	$0.89 \pm 0.09\,\mathrm{s}^{-1}$	$1.23 \pm 0.22\,\mathrm{s}^{-1}$	$1.46 \pm 0.12\,\mathrm{s}^{-1}$
$T_{2,obs}$	85 ± 4 ms	91 ± 4 ms	120 ± 5 ms	98 ± 5 ms

Chapter 4

Methods

4.1 Imaging Protocol

The imaging sequences composing this experimental protocol were developed, implemented, and validated by Sled and Pike [77, 71]. As summarized in Figure 4.1, the protocol comprises conventional whole-brain high-resolution scans, single-slice relaxometry and MT-weighted acquisitions, and finally, field maps for intensity non-uniformity corrections of quantitative data. A complete exam requires about 45 minutes of actual scan time.

All measurements, with exception of the high-resolution scans, focused on a 7-mm axial slice at the level of the corpus callosum, with 2×2 mm in-plane resolution. Imaging was performed on a 1.5 T Siemens Magnetom Vision clinical scanner (Siemens Medical Systems, Erlangen, Germany), using the standard head coil. For 11 subjects (6 patients, 5 controls), a solution of 0.11 mM $MnCl_2$ and 49 mM NaCl was included in the field-of-view. This reference solution ($T_1 = 1.06 \pm 0.04$ s, $T_2 = 149 \pm 5$ ms) was used in absolute pool size quantification.

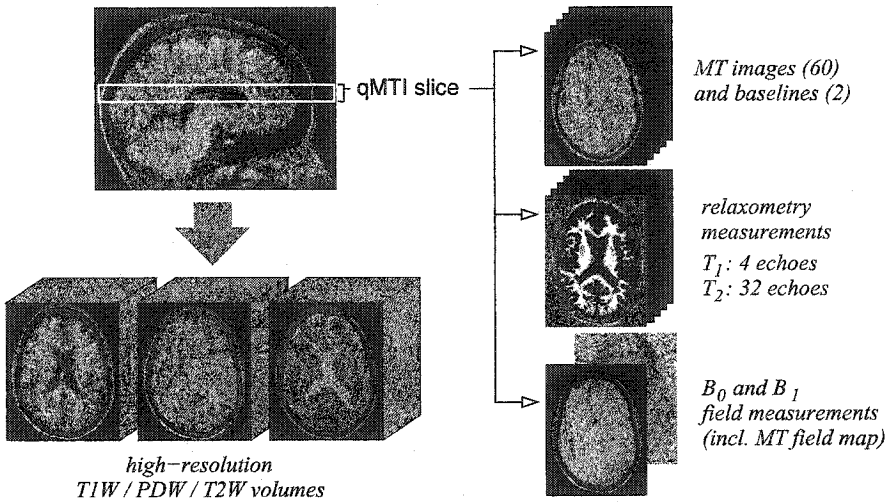

Figure 4.1: Schematic of the data acquisition process, showing the qMTI slice position and a summary of data collected using the protocol.

High Resolution Scans

The high resolution whole brain scans provide axial T_1, T_2, and PD-weighted data, for anatomical localization, ROI definition and lesion identification. The T_1-weighted scan was acquired using a 3D spoiled gradient echo (GRE) sequence (TR / TE / α = 22 / 10 ms / 30°), providing whole brain coverage in 80 2-mm slices, with 1 × 1 mm in-plane resolution. The T_2 and PD-weighted images were acquired within the same turbo spin echo (TSE) protocol (TR / TE_1 / TE_2 = 2800 / 22 / 90 ms), and provided 16 2-mm slices (0.5 mm gap), with 1 × 1 mm in-plane resolution.

Relaxometry

Independent relaxometry measurements of the free pool are necessary for two reasons. First, a measurement of $T_{1,obs}$ is required to complete the data set needed for MT model

parameter estimation, as stated in Chapter 3. Second, an independent measurement of $T_{2,obs}$ was collected both for completeness and comparison with $T_{2,f}$ estimates obtained from the full model fits.

$T_{2,obs}$ was measured using a 32-echo CPMG sequence (TR / TE = 2000 / 10 ms). Non-selective, rectangular 1-ms pulses were used to refocus transverse magnetization. A crusher gradient scheme alternating in sign and decreasing in magnitude for each inversion pulse [34] helps reduce the effect of main and RF field inhomogeneities. The observable T_2 ($T_{2,obs}$) should correspond to the free pool $T_{2,f}$, given the very small value of $T_{2,r}$ and the absence of exchange of transverse magnetization. This multi-echo spin-echo sequence is illustrated in Figure 4.2, showing the crusher gradient schemes as well.

Apparent T_1 ($T_{1,obs}$) measurements were performed using a Look-Locker multi-echo sequence, a fast T_1 relaxometry technique. As illustrated in Figure 4.3, the Look-Locker sequence consists of a non-selective composite $90x-180y-90x$ inversion pulse, followed after some time TI_1 by a number N of small angle slice selective excitations and GRE readout, each separated by an interval TI_2.

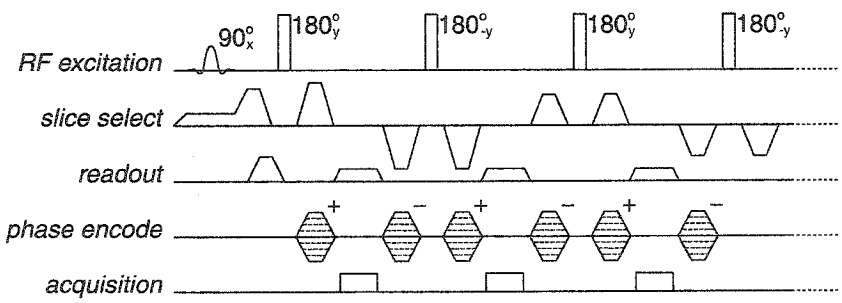

Figure 4.2: Illustration of multi-echo spin-echo sequence for quantitative T_2 data acquisition, showing RF pulses, gradient schemes and data acquisition (from [78]).

The Look-Locker sequence parameters were selected in the following way. TR was chosen long enough with regards to most T_1 values to optimize measurement precision (TR / TE = 2000 / 12 ms). TI_1 was set to be as short as possible to take full advantage of the inversion recovery, while TI_2 was selected as long as possible to span the greatest interval of recovery (TI_1 / TI_2 = 15 / 495 ms). In selecting the number of excitations, $N = 4$ were used to balance the trade-off between: too many, influencing the relaxation of long T_1 species; and too few, decreasing the precision of short T_1 estimates. A flip angle of $\beta = 20°$ was selected, to optimize SNR and recovery rate.

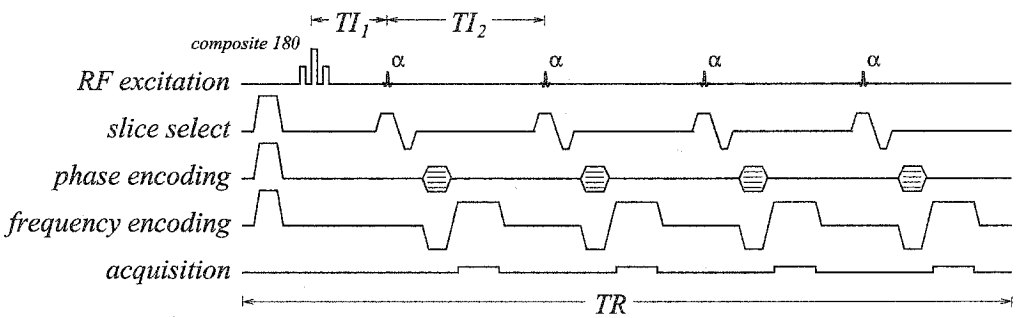

Figure 4.3: Illustration of Look-Locker imaging for quantitative T_1 data acquisition.

MT Imaging

Estimation of all five parameters of the binary spin-bath MT model – f, k_f, $R_{1,f}$, $T_{2,f}$, $T_{2,r}$ – requires at least 4 MT measurements and an independent $T_{1,obs}$ measurement. As proposed in the original protocol, we collected 60 MT measurements during each experiment, to maintain a unique and consistent set of results for each subject. Previous validation of the protocol had established the accuracy of the model.

These MT-weighted scans were acquired using a spoiled gradient-echo sequence (MT-SPGR), where the MT saturation pulse is followed by a low angle excitation pulse and readout at each repetition (see Fig. 3.3). 4 signal averages were acquired for each image. Any transverse magnetization produced by the MT pulse is eliminated by crusher gradients and RF spoiling. 10 seconds of MT pulsing was used to drive the system into steady-state prior to imaging. The protocol parameters are summarized in Table 4.1.

MT pulse offset frequencies ranged, in logarithmic steps, from 234.3 Hz to 80 kHz, and for two different pulse powers. Two MT pulse durations were used to improve precision of k_f estimates. Since the model and parameter estimation are based on relative changes due to MT, baseline scans were also acquired without MT saturation, with 8 signal averages. Example MT data from an ROI in human brain is shown in Figure 4.4.

Table 4.1: Parameters of the MT-weighted pulse sequences.

protocol	TR	excitation pulse angle	MT pulse angles	MT pulse duration	logarithmic frequency steps
I	25 ms	7°	142°, 710°	10.24 ms	20
II	50 ms	10°	283°, 1132°	20.48 ms	10

An important modification was brought to protocol II relative to its previous implementation, in order to accommodate RF hardware problems (aging RF amplifier tube) encountered prior to beginning the study. The RF hardware was unable to maintain the high-power level over the entire MT pulse duration, and so a number of options were considered: lengthening the TR, decreasing the MT pulse duration, and modifying the pulse

flip angle. Modifying the flip angle yielded no change. A longer TR solved the problem, but at a significant increase in scan time. Finally, the MT pulse duration was decreased from 30.72 ms to 20.48 ms, and the pulse flip angle was decreased accordingly to maintain equivalent average saturation RF power.

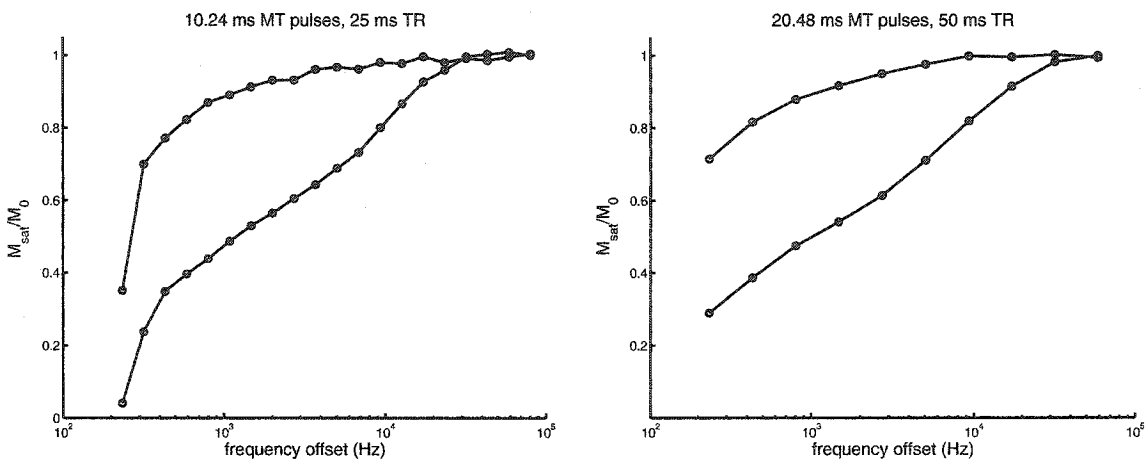

Figure 4.4: Example MT-weighted data from an ROI in human brain, showing distribution of relative MT-weighted data points against offset frequency (index), for both pulse powers and pulse durations used.

Intensity Non-Uniformity Corrections

Quantitative MRI measurements are affected by smooth intensity variations observed in MR images. These intensity non-uniformities are the result of RF field inhomogeneity, non-uniform receive-coil sensitivity, poor slice selection profiles, as well as electrodynamic interaction of the fields with the subject. Corrections should to be applied to all quantitative measurements to account for these inhomogeneities.

Different approaches exist to correct for non-uniformity. Some are based on independent measurement or physical modeling of field variations, while others use statistical methods to base the correction on the actual data. The method used in this work is based on measurements of field variations, during the exam.

The main magnetic field B_0 is mapped employing the shifted readout phase difference method [79]. A pair of fast gradient-echo acquisitions (TR / TE = 53 / 10 ms), with different readout times, are used. The readout shift T_D of 4.48 ms is based on the observed off-resonance shift of lipids at 1.5 T (223 Hz), corresponding to a 2π phase shift bringing lipids in phase with adjacent water. This sequence is illustrated in Figure 4.5. Furthermore, the use of strong crushing gradients in the MTSPGR sequences leads to the creation of eddy currents within the subject, causing local shifts in the apparent field strength. A separate B_0 map is acquired for these sequences, using a modified MTSPGR sequence (without MT pulses) adapted to make use of the shifted readout technique.

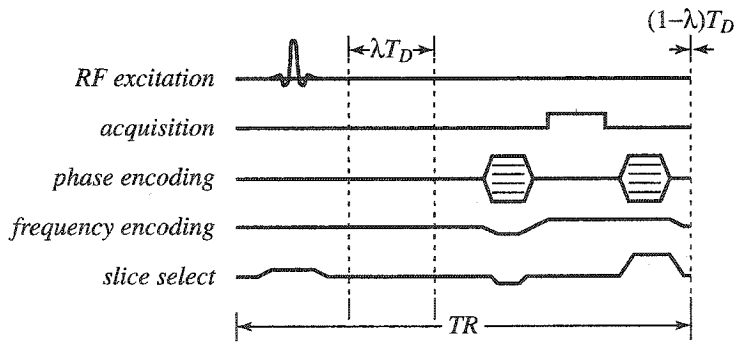

Figure 4.5: Illustration of main magnetic field mapping pulse sequence. The readout shift is obtained by adding the delay time T_D to the echo time, while TR remains constant – corresponding to λ taking the value 0 or 1 (from [80]).

The RF field mapping sequence consists of a non-selective rectangular pulse of flip angle η followed after some time $\tau/2$ by a fast spin-echo readout – a slice-selective $\pi/2$ pulse followed by a train of slice selective π refocusing pulses separated by intervals τ, as shown in Figure 4.6. A second image is acquired with the angle η doubled (2η). The ratio of the two images I_2/I_1 is then related to the flip angle η of the first pulse. We used a nominal flip angle of $\eta = 33°$ ($2\eta = 66°$), and a 7-echo TSE readout (TR / TE = 2000 / 15 ms).

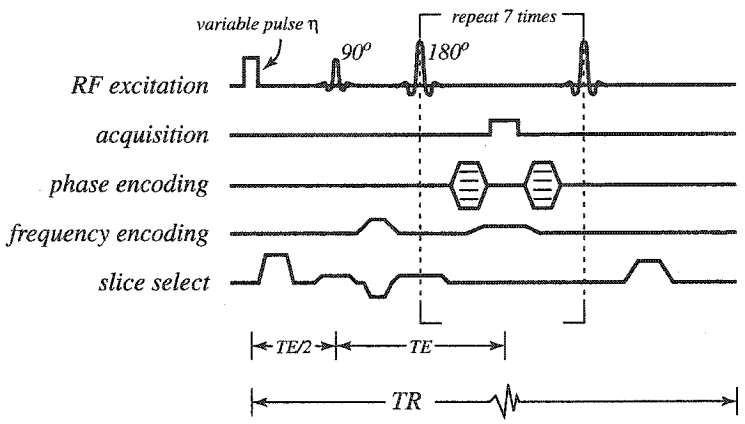

Figure 4.6: Illustration of RF field mapping pulse sequence. The initial pulse η has values of 33° and 66° (from [80]).

4.2 Parameter Estimation and Extraction

Estimation of Apparent Relaxation Times

Processing of relaxometry data is relatively straightforward. T_2 data was fitted with a two-parameter exponential decay equation yielding $T_{2,obs}$ and a scaling factor S_0 (Equation 4.1). S_0 is used later in the absolute quantification of the free and restricted pool magnetization.

$$S\left(\mathrm{TE}\right) = S_0 \mathrm{e}^{\left(-\mathrm{TE}/T_{2,obs}\right)} \tag{4.1}$$

T_1 relaxometry data was fitted with the signal equation for a Look-Locker sequence [71]. Let α and β be the flip angles of the inversion and excitation pulses, and TI_2 be the interval between excitations. The longitudinal magnetization after the n^{th} excitation pulse, M_n, is given by Equation 4.2, where $c_\beta = \cos\beta$, $E_2 = \exp(-\mathrm{TI}_2/T_1)$, and $F = (1 - E_2)/(1 - c_\beta E_2)$.

$$M_n = M_{eq}[F + (c_\beta E_2)^{n-1}(Q - F)] \tag{4.2}$$

$$Q = \frac{F c_\alpha c_\beta E_r E_1 [1 - (c_\beta E_2)^{N-1}] + c_\alpha E_1 (1 - E_r) - E_1 + 1}{1 - c_\alpha c_\beta E_r E_1 (c_\beta E_2)^{N-1}} \tag{4.3}$$

Note also that $c_\alpha = \cos\alpha$, $E_1 = \exp(-\mathrm{TI}_1/T_1)$, $E_r = \exp(-t_r/T_1)$, t_r being the interval between the last excitation pulse and the following inversion pulse. A least-squares algorithm implemented in the Python programming language was used for this fit.

MT Model Parameters

Estimation of the qMT parameters was done by combining results of the apparent T_{1obs} measurement to the MT data, and fitting to the model described in Chapter 3. Estimation was performed on a voxel-by-voxel basis using a simplex optimization technique and MATLAB software (The MathWorks, Natick, USA). Neighbouring voxels were used to set starting points for the optimization. Repetitive calculations of the saturation fraction S_f and the super-Lorentzian lineshape $G(\Delta)$ were avoided through the use of lookup tables. This yielded parametric maps of all five qMT model parameters: relative pool size f, exchange rate k_f, longitudinal relaxivity $R_{1,f}$, and spin-spin relaxation time constants $T_{2,f}$, and $T_{2,r}$. Voxels with an RMS error greater than 6% were re-fitted, and parametric maps were constructed on a voxel-by-voxel basis by selecting the set of results from the fit with minimum error.

After correcting for T_1 weighting and non-uniformities, an estimate of absolute proton density of the free pool, PD_f, was obtained by normalizing to the signal obtained from the water reference vial, in the 11 subjects where the standard was present. The absolute restricted pool proton density PD_r is obtained by scaling PD_f by the relative pool size f.

MTR was calculated directly using a single point of MT data. The MTR point was chosen to match as closely as possible the standard MT acquisition sequence of the Siemens scanner: we selected the acquisition corresponding to an offset frequency $\Delta = 1478.3$ kHz, and MT pulse duration $\mathrm{T}_{MT} = 10.24$ ms and an MT pulse angle of 568°. MTR is calculated as in Equation 3.2.

Intensity Corrections

As previously discussed, the main field is mapped using the shifted readout phase difference method. The B_0 map is calculated from the phase difference between the two acquisitions as in Equation 4.4, yielding the frequency offset from resonance of the carrier frequency used to demodulate the signal.

$$B_0 = \frac{\arg I_2 - \arg I_1}{2\pi T_D} \tag{4.4}$$

The RF field is also measured using two acquisitions, both comprising a non-selective preparation pulse, the first of angle η, and the second of angle 2η. This angle η is related to the ratio $R = I_2/I_1$ of the two images by Equation 4.5.

$$\eta = \cos^{-1}\left(\frac{R}{4} \pm \frac{1}{4}\sqrt{R^2+8}\right) \tag{4.5}$$

Normalizing the map of computed η by its nominal value produces a field map, and this map can be used to correct nominal pulse angles in other acquisitions.

For the T_2 measurements, it is assumed that the spoiling scheme used during the acquisition is efficient, so that unwanted signal components are eliminated. In this approximation, errors in the RF pulse angle and resonance shifts result in fractional attenuation of the measured signal with each refocusing inversion pulse, by a factor f. The signal at the n^{th} echo is thus:

$$S_n = S_0 \mathrm{e}^{-n\tau/T_2} f^n, \tag{4.6}$$

such that the true value of T_2 is related to the observed $T_{2,obs}$ by the following equation:

$$T_2 = \left(\frac{1}{T_{2,obs}} + \frac{\ln f}{\tau} \right)^{-1} \tag{4.7}$$

For imperfect inversion pulses, the attenuation factor is given by

$$f = sin^2 \left(\beta/2 \right), \tag{4.8}$$

where β is the measured flip angle of the refocusing pulse, as corrected using the B_1 field map.

Off-resonance effects on rectangular inversion pulses, such as those used in our experiment, lead to a slightly more complex attenuation factor. Considering the system in a reference frame rotating at the carrier frequency of the pulse (at an offset Δ from resonance), a rectangular pulse of duration t and nominal flip angle α will rotate the spins through an angle δ about an axis at an angle ϕ from the orientation of the main magnetic field (z), given in Equations 4.9 and 4.10. We can work out the attenuation factor for such a pulse to be given by the expression in Equation 4.11. A schematic of the data processing pipeline, producing relaxometry and quantitative MT results, is presented in Figure 4.7.

$$\delta = \sqrt{\alpha^2 + (2\pi\Delta t)^2} \tag{4.9}$$

$$\phi = \frac{\pi}{2} - \tan^{-1} \left(\frac{2\pi\Delta t}{\alpha} \right) \tag{4.10}$$

$$f = \sin^2 \left(\frac{\delta}{2} \right) \sin^2 \left(\phi \right) \tag{4.11}$$

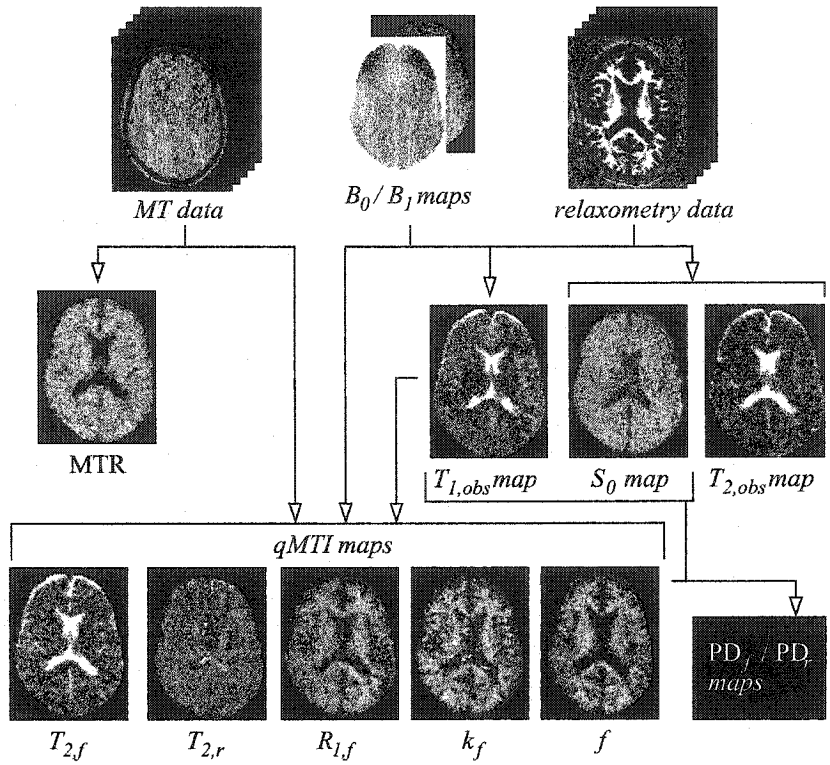

Figure 4.7: Schematic summary of data processing pipeline: MTR and qMTI parameters, relaxometry, and field inhomogeneity corrections.

Tissue Classification

For regional study of of qMT parameters, multiple regions-of-interest (ROIs) were defined by manual segmentation. This segmentation was performed by the same neuroradiologist in all subjects. In all patients, lesions were also identified, numbered, and dated based on scan history. Anatomical structures that were identified in each subject are:

- *white matter*
  - frontal and occipital white matter (left and right)
  - corpus callosum (genu and splenium)
  - anterior and posterior forceps (left and right)
  - posterior and anterior limb of internal capsule (left and right)

- *grey matter*
  - caudate (left and right)
  - putamen (left and right)
  - frontal and occipital cortical grey matter (left and right)

Semi-automatic tissue segmentation was performed for each subject using in-house software developed by Simon J. Francis[1]. The software employs an intensity-based algorithm for tissue classification according to T_1, T_2, and PD weighting on high-resolution scans. Voxels are classified as either white matter, grey matter, cerebro-spinal fluid, or MS lesion. First, a K-means classifier is applied to a training set of image voxels to produce clusters of classified data. These clusters are then manually screened and corrected until a final lookup table can be produced based on MRI intensity. This lookup table is then used by a Bayesian classifier to perform the automatic voxel-by-voxel segmentation.

The segmentation thus provided separate white matter, grey matter, and CSF maps. Lesion masks were produced using the manual segmentation. In some subjects, only partial brain coverage was available in T_2/PD-weighted data, so additional manual corrections had to be to applied the final tissue classification.

The tissue maps were then combined with the manually drawn ROIs, and then resampled to the low-resolution qMTI slice. Thresholding of the low-resolution voxels for tissue purity at 80 % yielded the final masks used for data extraction. The ROI and lesion labeling process, combined to the semi-automatic tissue classification, yields the set of derived labels used for extraction of results, as is presented in Figure 4.8. Voxels where the RMS fit error was greater than 6 % were excluded from the analysis.

[1]MRS unit, McGill University, Montreal Neurological Institute, Montreal.

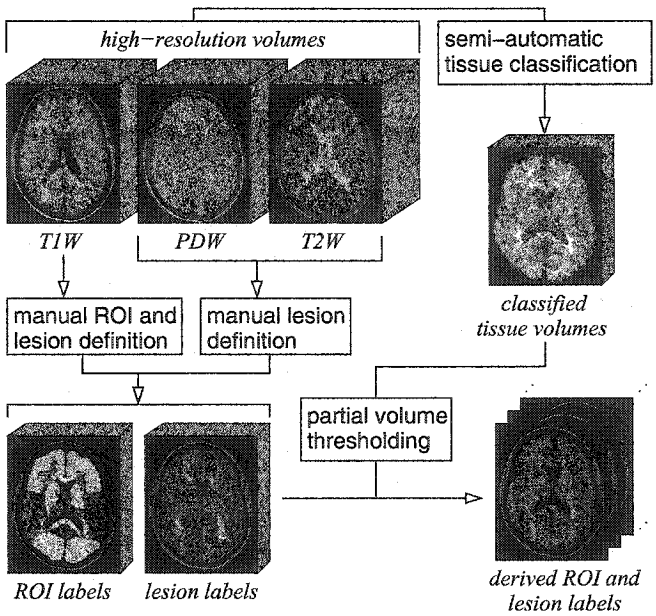

Figure 4.8: Schematic illustrating the production of derived ROI and lesion labels: manually identified regions are thresholded to 80% purity using data from the tissue classification.

4.3 Subject Cohort

The subject cohort consisted of 10 MS patients and 7 healthy controls. The patients were all volunteers recruited from the MS clinic at the Montreal Neurological Hospital (Montreal), and the controls were all healthy, age-matched volunteers from the university. Ethics approval was obtained from the McGill Research Ethics Board for the quantitative MTI protocol (see Appendix A). Informed consent was obtained from all subjects.

Of the MS patients, 5 were RR and 5 SP. Mean age was 34.6 $\pm$ 10.9 years [range 22-49] for the RR patients, and 43.6 $\pm$ 10.6 years [range 34-57] for the SP patients. The controls were recruited within the MNI, and their mean age was 37.6 $\pm$ 10.8 years [range 24-54] (see Table 4.2). A single-factor ANOVA test revealed no significant age difference between

controls and patients ($F = 0.080$, $p = 0.78$).

Patients underwent clinical evaluation on the day of the MRI exam, all performed by the same neurologist, and were given a score on the EDSS (0-10). These are summarized in Table 4.3, along with records of disease duration.

Table 4.2: Characteristics of the subject cohort: numbers by gender, subject group, and totals.

	female	male	**Total**	Age (yrs.)	
				mean ± std. dev.	*range*
RR	3	2	5	34.6 ± 10.9	22 - 49
SP	2	3	5	43.6 ± 10.6	34 - 57
All patients	5	5	**10**	39.1 ± 11.3	24 - 54
Controls	1	6	**7**	37.6 ± 10.8	24 - 54
Total	6	11	**17**	38.5 ± 10.7	22 - 57

Table 4.3: Disease duration and EDSS of MS patients.

	Duration (yrs.)		EDSS	
	mean ± std. dev.	*range*	*mean ± std. dev.*	*range*
RR	6 ± 3 yrs.	3 - 10	2.2 ± 1.2	1 - 4
SP	15 ± 7 yrs.	6 - 26	6.7 ± 1.6	5.5 - 9.5
All patients	10 ± 7 yrs.	3 - 26	4.5 ± 2.7	1 - 9.5

Chapter 5

Results

After collecting and processing the data, estimates were extracted using the derived ROI labels: these results are presented in this chapter. First, MT model parameter estimates are presented in tissue of healthy controls, for validation of the measurements and subsequent comparison with pathological values. Next, values in normal-appearing tissue of MS patients are presented. Finally, estimated parameters are given for MS lesions.

Throughout the chapter, results are analysed statistically within categories (normal tissue in controls, normal-appearing tissue in patients, lesions) for regional variations. Values in MS are compared to normals. The relationship between exchange rate k_f and macromolecular and liquid pool size measures (f, PD_r, and PD_f) is explored, and the role of each qMTI parameter in the MTR is investigated.

Because of assumptions made in calculating mean values of the parameter estimates over ROIs and across subjects, the variances reported reflect only the measurement precision, not model fitting errors.

5.1 MT Properties of Tissue in Normal Controls

Seven healthy volunteers were scanned using the protocol described in Chapter 4. For each subject, the combination of manual and automatic segmentation described in Section 4.2 was used to define labels for 22 anatomical regions, including left/right and grey/white distinctions. Manual labels were re-mapped to the low resolution qMT images and thresholded to exclude voxels with less than 80% of white or grey matter, in order to produce the derived labels.

Normal values of relaxation time constants, magnetization transfer ratio, and estimated MT parameters of both pools are presented in this section. We have reported some of these values previously in conference abstract form [81]. These measurements in healthy controls will serve both for purposes of validation, and for comparison with pathological values observed in MS. Table 5.1 presents normal values for the *conventional* MRI measures of $T_{1,obs}$ and $T_{2,obs}$, as well as the measure of magnetization transfer ratio, MTR.

Estimates of the MT parameters of both pools are listed in Table 5.2: the fractional pool size f, the exchange rate k_f, the free pool longitudinal relaxation constant $R_{1,f}$ and spin-spin relaxation time constant $T_{2,f}$, as well as the spin-spin relaxation time constant of the restricted pool $T_{2,r}$.

For five of the seven healthy controls, a water standard doped with paramagnetic salt was included in the field of view (see Section 4.1). The inclusion of a water standard enabled calculation of absolute proton density of the free pool (PD_f). Scaling this value by the fractional pool size f then yielded absolute proton density in the restricted pool (PD_r) as well. Estimation results are presented in Table 5.3.

Table 5.1: Mean and standard deviation of relaxation time constant estimates ($T_{1,obs}$, $T_{2,obs}$) and magnetization transfer ratio MTR in normal controls, by region-of-interest.

	$T_{2,obs}$ (ms)	$T_{1,obs}$ (s)	MTR (%)
frontal WM*	74.7 ± 3.7	0.614 ± 0.022	52.2 ± 1.2
occipital WM*	85.9 ± 2.5	0.621 ± 0.023	51.9 ± 1.4
corpus callosum			
genu	74.8 ± 2.7	0.555 ± 0.016	52.0 ± 1.2
splenium	91.3 ± 6.5	0.581 ± 0.016	50.3 ± 2.6
internal capsule			
posterior limb*	88.9 ± 4.8	0.615 ± 0.027	51.1 ± 1.6
anterior limb*	75.8 ± 2.5	0.637 ± 0.035	50.2 ± 1.4
posterior forceps*	91.7 ± 5.5	0.594 ± 0.019	51.3 ± 1.7
anterior forceps*	75.0 ± 3.7	0.572 ± 0.020	52.5 ± 1.4
caudate*	95.5 ± 18.0	1.008 ± 0.082	43.7 ± 2.3
putamen*	75.8 ± 2.3	0.859 ± 0.036	47.0 ± 1.4
frontal GM*	88.7 ± 4.3	1.061 ± 0.061	46.9 ± 1.5
occipital GM*	89.2 ± 3.9	0.968 ± 0.053	48.6 ± 1.7
white matter (all)	82.3 ± 2.4	0.619 ± 0.018	51.5 ± 1.3
grey matter (all)	91.5 ± 3.3	1.022 ± 0.051	46.8 ± 1.5

$\star$ indicates regions identified in both hemispheres. Values are aggregates of left and right data.

5.1.1 Regional variations in normal controls

Left and right anatomical structures were compared using a two-way ANOVA, which demonstrated no significant left/right differences in any of the quantitative parameters for both grey and white matter. Consequently, data presented in Tables 5.1 to 5.3 are aggregate data of left and right structures. After combining left and right regions of white matter, an ANOVA test revealed that all of the measures except PD_f showed highly significant differences ($p < 0.01$) within the set of white matter regions. For grey matter regions, all mea-

Table 5.2: Mean and standard deviation two-pool MT parameter estimates in normal controls, by region-of-interest.

	f(%)	k_f (s)	$T_{2,r}$ (μs)	$T_{2,f}$ (ms)	$R_{1,f}$ (s^{-1})
frontal WM*	12.7 ± 1.1	4.37 ± 0.38	11.04 ± 0.33	26.4 ± 2.2	1.727 ± 0.067
occipital WM*	12.0 ± 0.9	3.69 ± 0.37	11.20 ± 0.47	26.4 ± 1.3	1.700 ± 0.067
corpus callosum					
genu	14.2 ± 1.1	5.05 ± 0.35	9.86 ± 0.39	25.4 ± 1.5	1.925 ± 0.064
splenium	12.7 ± 1.4	3.91 ± 0.69	10.01 ± 0.24	28.0 ± 2.9	1.822 ± 0.057
internal capsule					
posterior limb*	12.0 ± 1.0	3.70 ± 0.52	11.78 ± 0.59	28.1 ± 2.5	1.708 ± 0.082
anterior limb*	10.6 ± 1.3	3.90 ± 0.61	10.46 ± 0.67	28.0 ± 2.5	1.643 ± 0.096
posterior forceps*	12.6 ± 1.2	4.18 ± 0.45	10.03 ± 0.27	27.4 ± 2.0	1.780 ± 0.065
anterior forceps*	14.0 ± 1.1	4.76 ± 0.51	10.48 ± 0.34	25.4 ± 1.1	1.868 ± 0.073
caudate*	6.0 ± 0.7	1.69 ± 0.33	9.82 ± 0.46	47.5 ± 16.9	1.007 ± 0.074
putamen*	7.0 ± 0.4	2.50 ± 0.22	10.26 ± 0.42	37.0 ± 2.9	1.181 ± 0.053
frontal GM*	6.4 ± 0.5	2.27 ± 0.28	9.90 ± 0.38	43.0 ± 4.7	0.967 ± 0.054
occipital GM*	7.0 ± 0.6	2.30 ± 0.34	10.04 ± 0.44	38.2 ± 2.4	1.071 ± 0.062
white matter (all)	12.2 ± 0.9	3.97 ± 0.36	10.96 ± 0.32	27.2 ± 1.5	1.713 ± 0.052
grey matter (all)	6.6 ± 0.5	2.15 ± 0.22	9.96 ± 0.41	41.9 ± 3.7	1.010 ± 0.051

$\star$ indicates regions identified in both hemispheres. Values are aggregates of left and right data.

sures except PD_f, PD_r and $T_{2,f}$ showed significant regional variations ($p < 0.05$). Thus, the only parameter to show no regional variation within grey or white matter was PD_f. When considering global values of both tissue types (white and grey matter), all parameters including PD_f showed highly significant differences ($p = 0.05$ for PD_f, $p < 0.0004$ for all others).

Table 5.3: Estimates of absolute proton density in free (PD_f) and restricted (PD_r) pools in normal controls, by region-of-interest.

	PD_f	PD_r
frontal WM*	0.662 ± 0.054	0.085 ± 0.008
occipital WM*	0.646 ± 0.057	0.079 ± 0.008
corpus callosum		
genu	0.627 ± 0.048	0.091 ± 0.010
splenium	0.619 ± 0.053	0.082 ± 0.014
internal capsule		
posterior limb*	0.626 ± 0.067	0.075 ± 0.007
anterior limb*	0.692 ± 0.050	0.075 ± 0.008
posterior forceps*	0.625 ± 0.051	0.081 ± 0.011
anterior forceps*	0.647 ± 0.048	0.092 ± 0.009
caudate*	0.761 ± 0.053	0.046 ± 0.007
putamen*	0.769 ± 0.059	0.052 ± 0.005
frontal GM*	0.730 ± 0.054	0.047 ± 0.006
occipital GM*	0.732 ± 0.054	0.052 ± 0.006
white matter (all)	0.654 ± 0.054	0.081 ± 0.009
grey matter (all)	0.736 ± 0.055	0.049 ± 0.006

$\star$ indicates regions identified in both hemispheres. Values are aggregates of left and right data.

5.1.2 Exchange rate and macromolecular pool size in normal controls

To explore the meaning of the exchange rate, k_f was tested for correlation with liquid and macromolecular pool size measures – f, PD_f, and PD_r. In order to include inter-subject variability in our comparison, the analysis included each ROI from each subject. k_f is plotted versus f for all ROIs in Figure 5.1. The results across all regions-of-interest are summarized in Table 5.4. When pooling grey and white matter regions, the correlations were strong for f, and PD_f, and strongly negative for PD_r.

When tissue types were considered separately however, a few differences were observed. f and k_f were only weakly correlated within both grey matter and white matter regions-of-interest. The correlation of k_f with PD_f disappeared in grey matter, while PD_r remained correlated with k_f. The reverse was seen in white matter, where k_f correlated with PD_f: this may explain the weaker correlation seen between k_f and f. This indicates that magnetization exchange rate k_f in healthy tissue generally depends on the macromolecular content. However, the relationship between f and k_f is diffuse, and the scatter seems to increase with fractional pool size as seen in Figure 5.1.

Table 5.4: Pearson-r correlation of k_f with pool size measures f, PD_f, and PD_r across regions-of-interest in healthy controls (p values in brackets). The data for f are plotted in Figure 5.1.

	r - all ROIs	r - WM ROIs	r - GM ROIs
f	0.86 (< 0.0001)	0.32 (0.002)	0.51 (< 0.0001)
PD_f	-0.65 (< 0.0001)	-0.30 (0.02)	0.09 (NS)
PD_r	0.77 (< 0.0001)	-0.03 (NS)	0.39 (0.02)

NS = non-significant, $p > 0.05$

5.1.3 MTR and the role of qMTI parameters in normal controls

Since one of our goals was also to study which qMTI parameters play a dominant role in the MTR, the measurements of MTR were tested for correlations with these parameters across regions of normal tissue. This exploration of the relationship between MTR and the qMTI parameters also included the effects of inter-subject variability. When compared to the quantitative measures, MTR was shown to correlate strongly with all quantitative MT model parameters except $T_{2,r}$, which correlated moderately, as shown in Table 5.5.

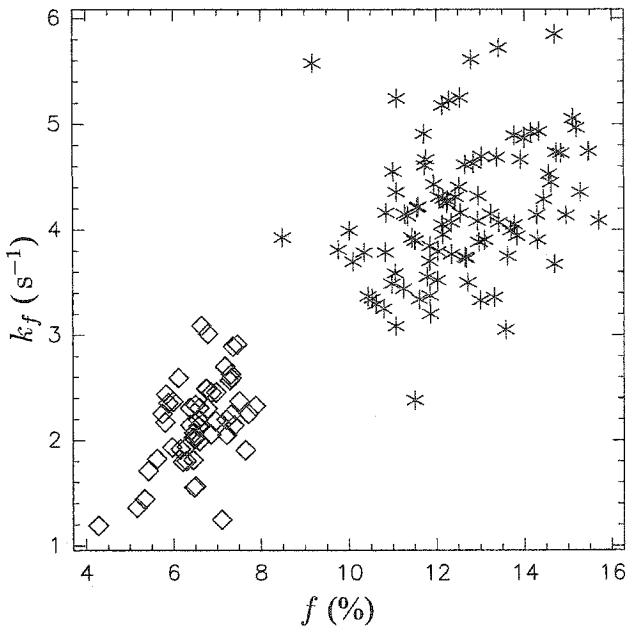

Figure 5.1: k_f as a function of f in normal controls, for white matter (*) and grey matter (◇), in individual ROIs. ROI averages across subjects are presented in Table 5.2.

However, if we look at the relationship between f and MTR as plotted in Figure 5.2, white and grey matter ROIs seem to belong to separate curves in the parameter space. The correlations are artificially high when pooling tissue types.

Regions-of-interest were thus considered separately, according to tissue type. In grey matter ROIs, MTR and f were strongly correlated. MTR correlated moderately with PD_r and k_f, but not with PD_f. In white matter ROIs, both the correlations of MTR with f and k_f were moderate; this supports the theory that MTR reflects both macromolecular pool size and the exchange rate in white matter. Also of note, the free pool relaxation rate constant $R_{1,f}$, demonstrated a significant correlation with MTR in both white and grey matter, indicating that this parameter also plays a role in determining MTR of healthy tissue.

Table 5.5: Pearson-r correlation of MTR with qMTI parameters across regions-of-interest in healthy controls (p values in brackets). The data for f are plotted in Figure 5.2.

	r - all ROIs	r - WM ROIs	r - GM ROIs
f	0.84 (< 0.0001)	0.59 (< 0.0001)	0.73 (< 0.0001)
PD_f	-0.60 (< 0.0001)	-0.31 (0.02)	-0.07 (NS)
PD_r	0.77 (< 0.0001)	0.26 (NS)	0.49 (0.002)
k_f	0.81 (< 0.0001)	0.42 (< 0.0001)	0.68 (< 0.0001)
$R_{1,f}$	0.81 (< 0.0001)	0.47 (< 0.0001)	0.39 (0.004)
$T_{2,f}$	-0.81 (< 0.0001)	-0.58 (< 0.0001)	-0.62 (< 0.0001)
$T_{2,r}$	0.41 (< 0.0001)	0.13 (NS)	0.11 (NS)

NS = non-significant, $p > 0.05$

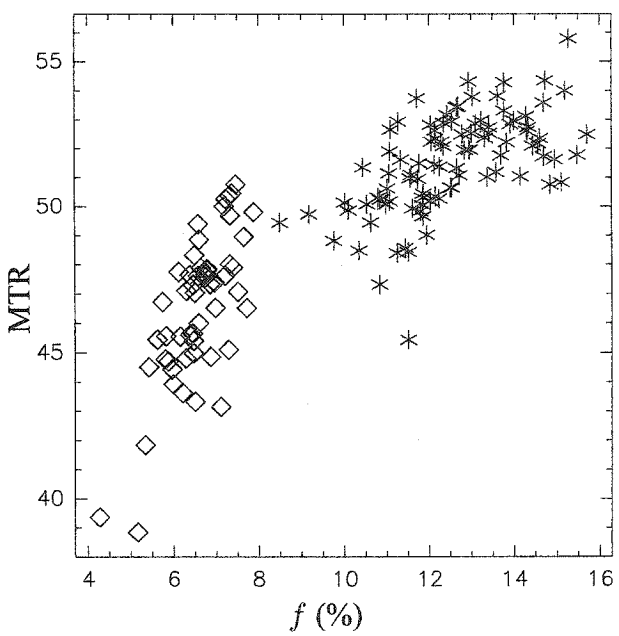

Figure 5.2: MTR as a function of fractional pool size f in normal controls, in individual ROIs of white matter (*) and grey matter (◇). Data averaged across subjects are presented in Tables 5.1 and 5.2.

5.2 Properties of Normal-Appearing Tissue in MS

Ten multiple sclerosis patients were scanned using the qMTI technique described in Chapter 4. This section reports values from normal-appearing tissue, both in grey and white matter. The study of normal-appearing tissue of these patients made use of the same 22 anatomical regions and classification method as in the previous section.

Estimates of relaxation time constants, magnetization transfer ratio, and estimated MT properties of both pools of normal-appearing tissue in MS are reported in this section. Table 5.6 presents these values for $T_{1,obs}$ and $T_{2,obs}$, as well as magnetization transfer ratio. Table 5.7 shows MT parameter estimates in both the free and restricted pools, across normal-appearing tissue structures of MS patients.

In six of the ten patients, the same water standard was included in the field of view, to provide estimates of absolute proton density of the free and restricted pools. These estimation results are presented in Table 5.8.

5.2.1 Regional variations in MS

As stated in Section 5.1.1, no significant left-right differences were observed in tissue structures of healthy controls. As there are no established reasons to believe that MS develops preferentially in one hemisphere or the other in a systematic way, the patient data was not analysed for left/right differences. Any differences should stem from the focal development of MS. Furthermore, supporting any claim of systematic hemispheric differences would require a much greater population sampling. Data presented in Tables 5.6 to 5.8 are thus combinations of left and right values.

Table 5.6: Mean and standard deviation relaxation time constant estimates ($T_{1,obs}$, $T_{2,obs}$) and magnetization transfer ratio MTR in normal-appearing tissue of MS patients, by region-of-interest.

	$T_{2,obs}$ (ms)	$T_{1,obs}$ (s)	MTR (%)
frontal WM*	79.0 ± 8.5	0.648 ± 0.049	51.1 ± 1.5
occipital WM*	88.1 ± 4.8	0.645 ± 0.039	51.5 ± 1.1
corpus callosum			
genu	82.8 ± 9.3	0.619 ± 0.044	50.1 ± 2.5
splenium	101.3 ± 13.5	0.645 ± 0.063	48.4 ± 1.9
internal capsule			
posterior limb*	91.9 ± 6.1	0.627 ± 0.024	51.1 ± 1.1
anterior limb*	78.7 ± 6.6	0.641 ± 0.037	50.4 ± 1.4
posterior forceps*	96.9 ± 8.4	0.637 ± 0.042	50.0 ± 1.3
anterior forceps*	80.8 ± 8.2	0.621 ± 0.045	51.0 ± 1.9
caudate*	95.3 ± 20.0	1.005 ± 0.049	42.5 ± 3.2
putamen*	79.6 ± 6.9	0.855 ± 0.045	47.1 ± 0.9
frontal GM*	89.8 ± 8.2	1.050 ± 0.046	46.3 ± 1.4
occipital GM*	90.2 ± 8.0	0.932 ± 0.050	49.2 ± 1.2
white matter (all)	92.9 ± 6.2	0.994 ± 0.035	47.0 ± 0.9
grey matter (all)	87.5 ± 6.1	0.659 ± 0.043	50.4 ± 1.1

$\star$ indicates regions identified in both hemispheres. Values are aggregates of left and right data.

Combining left and right regions of tissue, an ANOVA test indicated that all parameters demonstrated highly significant differences when comparing global values of white and grey matter ($p < 0.002$), with the exception of $T_{2,obs}$ ($p = 0.06$). The test showed significant differences ($p < 0.01$) for all parameters among some grey matter regions. Furthermore, some significant differences ($p < 0.05$) were observed among white matter regions, for all of the parameters except $R_{1,f}$, $T_{1,obs}$, and PD_r. Most interesting was what can be characterised as a "blurring" effects observed in $R_{1,f}$ and PD_r in normal-appearing tissue of MS

Table 5.7: Mean and standard deviation two-pool MT parameter estimates in normal-appearing tissue of MS patients, by region-of-interest.

	$f(\%)$	k_f (s)	$T_{2,r}$ (μs)	$T_{2,f}$ (ms)	$R_{1,f}$ (s^{-1})
frontal WM*	11.9 ± 1.5	4.05 ± 0.72	10.82 ± 0.61	28.8 ± 3.5	1.628 ± 0.145
occipital WM*	11.0 ± 1.1	3.48 ± 0.59	10.91 ± 0.65	28.4 ± 2.6	1.624 ± 0.108
corpus callosum					
genu	12.0 ± 1.9	4.19 ± 0.92	9.92 ± 0.50	29.7 ± 3.6	1.709 ± 0.150
splenium	10.7 ± 1.1	3.08 ± 0.68	9.57 ± 0.51	33.4 ± 5.6	1.631 ± 0.160
internal capsule					
posterior limb*	11.8 ± 0.9	3.51 ± 0.51	11.70 ± 0.48	29.0 ± 2.8	1.673 ± 0.073
anterior limb*	10.7 ± 1.5	3.59 ± 0.63	10.87 ± 0.43	28.8 ± 4.0	1.630 ± 0.110
posterior forceps*	11.0 ± 1.3	3.50 ± 0.63	9.82 ± 0.65	30.9 ± 3.7	1.646 ± 0.124
anterior forceps*	12.3 ± 2.1	4.30 ± 0.88	10.11 ± 0.47	28.7 ± 3.8	1.706 ± 0.155
caudate*	5.5 ± 0.6	1.65 ± 0.35	9.45 ± 0.63	46.0 ± 5.6	1.000 ± 0.052
putamen*	7.5 ± 0.6	2.29 ± 0.30	10.09 ± 0.54	37.8 ± 2.6	1.189 ± 0.067
frontal GM*	6.4 ± 0.6	2.34 ± 0.51	9.75 ± 0.53	44.6 ± 4.6	0.968 ± 0.052
occipital GM*	7.3 ± 0.5	2.36 ± 0.41	9.85 ± 0.50	38.0 ± 3.0	1.101 ± 0.066
white matter (all)	11.1 ± 1.2	3.54 ± 0.55	10.71 ± 0.60	30.3 ± 3.3	1.594 ± 0.119
grey matter (all)	6.7 ± 0.4	2.17 ± 0.38	9.82 ± 0.47	41.8 ± 2.6	1.031 ± 0.041

$\star$ indicates regions identified in both hemispheres. Values are aggregates of left and right data.

patients. Increased variance observed in these measurements in MS patients, caused by the presence of pathology, is eliminating the statistical difference between regions on the basis of these parameters.

5.2.2 Exchange rate and macromolecular pool size in MS

The dependence of the exchange rate k_f on pool size measures was also considered in MS patients. k_f showed the same strong correlations with macromolecular pool size measures

Table 5.8: Mean and standard deviation estimates of absolute proton density in free (PD_f) and restricted (PD_r) pools in normal-appearing tissue of MS patients, by region-of-interest.

	PD_f	PD_r
frontal WM*	0.662 ± 0.023	0.080 ± 0.012
occipital WM*	0.647 ± 0.021	0.072 ± 0.009
corpus callosum		
genu	0.633 ± 0.008	0.079 ± 0.013
splenium	0.619 ± 0.027	0.066 ± 0.008
internal capsule		
posterior limb*	0.627 ± 0.017	0.075 ± 0.008
anterior limb*	0.663 ± 0.027	0.072 ± 0.014
posterior forceps*	0.632 ± 0.026	0.072 ± 0.010
anterior forceps*	0.649 ± 0.016	0.084 ± 0.016
caudate*	0.757 ± 0.039	0.043 ± 0.007
putamen left*	0.753 ± 0.040	0.055 ± 0.007
frontal GM*	0.720 ± 0.025	0.046 ± 0.007
occipital GM*	0.711 ± 0.020	0.052 ± 0.005
white matter (all)	0.660 ± 0.024	0.074 ± 0.010
grey matter (all)	0.726 ± 0.025	0.049 ± 0.005

$\star$ indicates regions identified in both hemispheres. Values are aggregates of left and right data.

as in healthy controls: positive for f and PD_r, and negative for PD_f (Table 5.9). When considering tissue types separately, similar effects were again noted as in healthy controls. k_f correlated weakly with f in white and grey matter. k_f correlated moderately with PD_f in grey matter, while neither absolute proton density measures correlated with k_f in white matter. However, the power of the tests involving absolute proton densities was poor as data was only collected in a portion of the subjects. This similarity between healthy and normal-appearing tissue was reflected in the plot of k_f as a function of f, and so it is not included here.

Table 5.9: Pearson-r correlation of k_f with pool size measures f, PD_f, and PD_r across regions-of-interest in normal-appearing tissue of MS patients (p values in brackets). The data for f are plotted in Figure 5.3.

	r - all ROIs	r - WM ROIs	r - GM ROIs
f	0.74 (< 0.0001)	0.28 (0.002)	0.26 (0.03)
PD_f	-0.75 (< 0.0001)	-0.14 (NS)	-0.48 (0.0005)
PD_r	0.65 (< 0.0001)	0.09 (NS)	0.00 (NS)

NS = non-significant, $p > 0.05$

5.2.3 MTR and and the role of qMTI parameters in MS

As done for healthy controls, we correlated mean MTR with mean qMTI parameters across regions-of-interest, this time in normal-appearing tissue. When considering all white and grey matter ROIs, MTR was shown to correlate strongly with all quantitative MT imaging parameters except $T_{2,r}$, which correlated moderately, as shown in Table 5.10. However, these correlations were artificially high due to the pooling of tissue types. As seen in Figure 5.3, grey and white matter ROIs appear to sit on separate curves, just as for healthy controls. The curves, however, appear to be closer than for normal controls (see Figure 5.3), and this is likely due to the smaller changes observed in normal-appearing grey matter of MS patients.

Regions were also considered according to tissue type. In grey matter ROIs, MTR showed similar correlations as for normals with f, k_f, $R_{1,f}$ and $T_{2,f}$. A significant negative correlation was observed between MTR and PD_f, whereas the correlation of MTR with PD_r observed in normals disappeared in patients. When considering white matter ROIs,

MTR correlated with f, k_f, $R_{1,f}$, and $T_{2,f}$ moderately, just as in healthy tissue. Unlike in normal-appearing grey matter regions-of-interest, MTR did not correlate with either of the absolute proton density measures. Interestingly, MTR was shown to correlate significantly with $T_{2,r}$ in both types of tissue, whereas this correlation between MTR and $T_{2,r}$ did not exist in healthy controls.

Table 5.10: Pearson-r correlation of MTR with qMTI parameters in normal-appearing tissue of MS patients, across regions of interest (p values in brackets). The data for f are plotted in Figure 5.3.

	r, all ROIs	r - WM ROIs	r - GM ROIs
f	0.80 (< 0.0001)	0.60 (< 0.0001)	0.77 (< 0.0001)
PD_f	-0.75 (< 0.0001)	-0.14 (NS)	-0.48 (0.0005)
PD_r	0.65 (< 0.0001)	0.09 (NS)	0.00 (NS)
k_f	0.73 (< 0.0001)	0.46 (< 0.0001)	0.58 (< 0.0001)
$R_{1,f}$	0.73 (< 0.0001)	0.44 (< 0.0001)	0.42 (0.0001)
$T_{2,f}$	-0.82 (< 0.0001)	-0.54 (< 0.0001)	-0.70 (< 0.0001)
$T_{2,r}$	0.51 (< 0.0001)	0.42 (< 0.0001)	0.31 (0.008)

NS = non-significant, $p > 0.05$

5.2.4 Comparison of normal-appearing and healthy tissue

Finally, values in normal-appearing tissue of MS patients were compared to those of healthy control parameter estimates. First, in order to obtain a global picture accounting for inter-subject variability in our exploration of differences between normal-appearing and healthy tissue, the data was first analysed with a two-way ANOVA for each measured and estimated parameter, comparing individual regions between patients and controls. In white matter, the

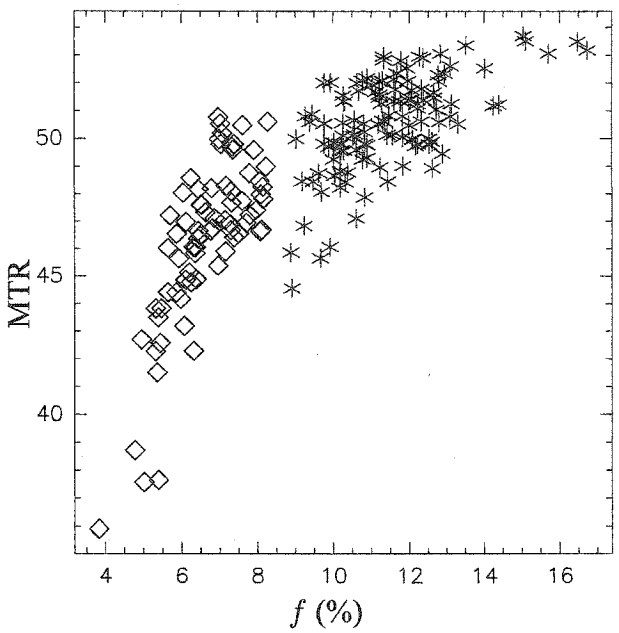

Figure 5.3: MTR as a function of fractional pool size f in normal-appearing tissue of MS patients, for white matter (*) and grey matter ($\diamond$) ROIs. These data are presented in Tables 5.6 and 5.7.

analysis revealed highly significant ($p < 0.0003$) differences between regions-of-interest in controls and patients, for all parameters except PD_f ($p = 0.75$). It is noted that differences in $T_{2,r}$ were considerably less significant ($p = 0.03$).

Differences observed in grey matter ROIs between patients and controls were few and borderline in $T_{2,r}$ ($p = 0.03$) and $T_{1,obs}$ ($p = 0.05$). Significant regional differences were detected, as previously mentioned in regional comparisons of parameters. Our two-way ANOVA did not reveal significant interaction between regions and subject group. In essence, this group of patients demonstrates significantly different tissue parameters from the healthy controls in normal-appearing regions of white matter, except in the transverse relaxation constant of the restricted pool, and interestingly, in the free pool absolute proton

density. The patient group was not observed to have significantly different qMTI parameters from healthy controls in normal-appearing grey matter regions.

Following the general analysis, the differences in mean values of each estimated parameter between patients and controls were examined for all regions-of-interest (those presented in Tables 5.1 through 5.3 and 5.6 through 5.8). Results of t-tests demonstrated significant differences ($p < 0.05$) as summarized in Table 5.2.4. Note that no grey matter structures demonstrated any significant differences between patients and controls.

Interestingly, the fractional pool size proved to be different in many white matter structures (genu and splenium of the corpus callosum, posterior and anterior forceps, occipital white matter) of MS patients when compared to healthy controls. MTR also demonstrated significant differences between controls and patients, in frontal white matter and in the forceps. In order to assess whether this difference reflected a change in semi-solid and/or water compartments, proton densities of the free and restricted pool were considered next: these did not show significant differences however (perhaps due to the smaller sample size in both patient and control groups), though some trends were observed for PD_r in occipital white matter, the posterior forceps, and the splenium of the corpus callosum.

Table 5.11: Summary of ROIs showing significant differences in a t-test between ROIs of healthy controls and normal-appearing tissue in MS patients ($p < 0.05$).

Parameter	**Region(s)**
MT ratio	frontal WM, forceps
fractional pool size f	genu/splenium, occipital WM, forceps
exchange rate k_f	genu/splenium, forceps
restricted pool $T_{2,r}$	anterior forceps
free pool $T_{2,f}$	frontal/occipital WM, genu/splenium, forceps
free pool $R_{1,f}$	frontal/occipital WM, genu/splenium, forceps
apparent $T_{2,obs}$	genu, anterior forceps
apparent $T_{1,obs}$	frontal/occipital WM, genu, forceps
proton densities PD_f, PD_r	PD_r different in splenium (smaller sample)

5.3 Properties of MS Lesions

Finally, results are presented in focal lesions of MS patients, as identified on high-resolution anatomical scans. From the 10 patients that were scanned, a total of 66 T_2-weighted hyperintensities were manually identified: 57 of these also had associated T_1 hypointensities. After tissue classification and partial volume thresholding, our analysis retained 28 T_2 lesions, of which 13 also appeared hypointense on the T_1-weighted scans.

For the purposes of this discussion, T_2-weighted hyperintensities shall be referred to as T_2-weighted lesions, consequently including all lesions. The subset of these lesions that are also T_1 hyperintensities are termed T_1-weighted lesions. It is important to note that the T_1-hypointense portion of a lesion does not generally extend to the same boundaries as the T_2-hyperintense region: the T_1 lesion normally corresponds to the core of the T_2 lesion. A third class of lesions will also be discussed: T_2-only lesions, those that occur strictly as hyperintensities on T_2-weighted scans, and not as T_1-weighted hypointensities.

Table 5.12 reports estimates of $T_{1,obs}$ and $T_{2,obs}$, as well as magnetization transfer ratio MTR, in all lesion types. Table 5.13 lists mean MT parameter estimates in both the free and restricted pools of lesions, for all lesion types. In patients where the water standard was included in the field of view, absolute proton density was calculated in the free and restricted pools. These estimation results are presented in Table 5.14.

Table 5.12: Mean and standard deviation relaxation time constant estimates ($T_{1,obs}$, $T_{2,obs}$) and magnetization transfer ratio MTR in MS lesions, by lesion type.

	$T_{2,obs}$ (ms)	$T_{1,obs}$ (s)	MTR (%)
T_1 lesions	189.8 ± 48.4	1.714 ± 0.363	33.9 ± 4.6
T_2-only lesions	175.1 ± 49.2	1.402 ± 0.311	35.3 ± 5.3
All (T_2) lesions	179.2 ± 49.8	1.493 ± 0.355	34.9 ± 5.1

5.3.1 MS lesions and healthy white matter

Comparison of our measurements in lesions to those in normal white matter show very significant ($p < 0.0001$) increases in apparent relaxation time constants $T_{1,obs}$, $T_{2,obs}$, and proton density PD_f, as well as decreases in MTR and the other qMTI parameters (f, k_f, PD_r, $T_{2,r}$, and $R_{1,f}$). The first exception to this observation was the parameter $T_{2,f}$ which demonstrated only a weakly significant difference ($p = 0.04$) between T_1-weighted lesions and normal white matter. This is inconsistent with the fact that these lesions have been defined as T_2 hyperintense, and furthermore, T_1 hypointense. Noting that $T_{2,obs}$ demonstrated

Table 5.13: Mean and standard deviation two-pool MT parameter estimates in MS lesions, by lesion type.

	f(%)	k_f (s)	$T_{2,r}$ (μs)	$T_{2,f}$ (ms)	$R_{1,f}$ (s^{-1})
T_1 lesions	2.8 ± 1.1	0.81 ± 0.43	7.83 ± 1.25	107.8 ± 105.7	0.598 ± 0.129
T_2-only lesions	3.6 ± 1.4	0.90 ± 0.42	8.09 ± 1.24	81.6 ± 29.2	0.741 ± 0.168
All (T_2) lesions	3.4 ± 1.4	0.86 ± 0.41	8.01 ± 1.24	89.2 ± 63.3	0.698 ± 0.169

very significant differences between lesions and healthy white matter, and that $T_{2,f}$ estimates were inconsistent with these measures of $T_{2,obs}$, the discrepancy can be attributed to the poor estimation of $T_{2,f}$ afforded by our calculations. PD_f was the only other parameter to show difference significance factors above $p = 0.0001$ (*e.g.* $p = 0.004$ for T_1 lesions).

Table 5.14: Mean and standard deviation estimates of absolute proton density in free (PD_f) and restricted (PD_r) pools in MS lesions.

	PD_f	PD_r
T_1 lesions	0.866 ± 0.092	0.026 ± 0.010
T_2-only lesions	0.813 ± 0.064	0.029 ± 0.011
All (T_2) lesions	0.833 ± 0.075	0.028 ± 0.010

5.3.2 Exchange rate and macromolecular pool size in lesions

In order to determine the dependence of magnetization exchange rate on the molecular composition of lesions, k_f was tested for correlations to f, PD_f, and PD_r, in all lesion types. k_f did not correlate at all with macromolecular and liquid content: only in the T_2-only lesion subset did k_f demonstrate a weak correlation with f ($r = 0.453$, $p = 0.02$). Recall that in normals and in normal-appearing tissue, k_f showed a weak dependence on liquid and macromolecular pool sizes. So, unlike in healthy controls and normal-appearing tissue of MS patients, k_f does not seem to show a relationship to tissue content in MS lesions.

5.3.3 The role of qMTI parameters in MTR of lesions

The relationship between MTR and the other quantitative parameters was also explored in lesions. MTR is plotted as a function of f in Figure 5.4, showing that for MTR values in the range of 35 - 45 % (recall that white matter MTR in normal controls = 51.5 $\pm$ 1.3 %), there was as much as a two-fold difference in the semi-solid/liquid ratio (f).

Our analysis considered mean values in individual lesions, and voxel-by-voxel values. When including all lesions, MTR showed a moderate correlation with f which held for both T_2-only and T_1 lesions (Table 5.15), as previously presented in [82]. This confirmed our belief that MTR is related but cannot be equated to macromolecular content. Voxel-based analysis confirmed these moderate correlations between f and MTR for all lesion types.

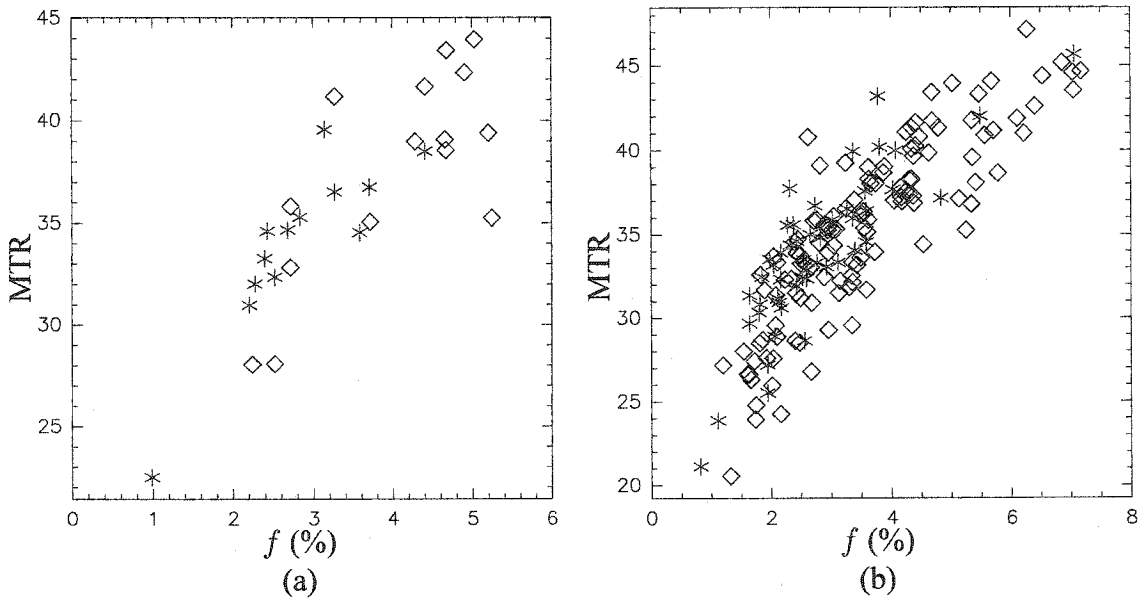

Figure 5.4: MTR as a function of fractional pool size f for T_1 (*) and T_2-only ($\diamond$) lesions: for lesion ROIs (a), and individual lesion voxels (b).

In order to study the dependence of MTR on absolute restricted pool content and the confounding effect of edema, MTR was also tested for correlation with absolute PD measures. MTR correlated strongly with PD_r in all lesion types (see Table 5.15), but did not correlate with PD_f. The same observations were made when considering voxel data. Furthermore, MTR showed no significant correlation with mean values of k_f in lesions. On a voxel basis, this was also true of T_1 lesion voxels; however, a correlation ($r = 0.76$, $p < 0.0001$) was observed for T_2-only lesion voxels.

5.3.4 Interpretation of T_1 hypointensity

As mentioned, there is a subset of T_2-hyperintense lesions that also appear hypointense on T_1-weighted scans. Also known as T_1 "black holes", these are believed to demonstrate more

Table 5.15: Pearson-r correlation of MTR with f, PD_r, and PD_f (p-values in brackets).

Parameter:	f	PD_r	PD_f
T1W lesions	0.87 (0.0001)	0.89 (0.02)	-0.54 (NS)
T2W-only lesions	0.74 (0.002)	0.87 (0.005)	0.06 (NS)
All lesions	0.77 (< 0.0001)	0.79 (0.0008)	-0.14 (NS)

pronounced tissue destruction [28]. To test this hypothesis, $T_{1,obs}$ hypointensity, averaged over each lesion, was also correlated with the set of potential measures of demyelination offered by the quantitative technique: f, k_f, $T_{2,r}$, and PD_r. To investigate the confound in the interpretation of T_1-weighted scans posed by the presence of edema and inflammation, $T_{1,obs}$ was compared to the measure of absolute liquid proton density, PD_f.

As we previously presented in conference abstract form [83], neither $T_{2,r}$ nor k_f correlated with $T_{1,obs}$ in T_1 hypointensities, while fractional pool size f showed a significant negative correlation (r = -0.82 , $p < 0.0006$) with $T_{1,obs}$. Neither PD_f or PD_r showed significant correlation with $T_{1,obs}$ ($r = 0.78$, $p = 0.07$, r = -0.78, $p = 0.07$ respectively); however, due to the fewer number of data points (six) the power of this test was comparatively poor. When considering all T_2 lesions in the test, the findings for f, k_f, and $T_{2,r}$ were the same as for T_1 black holes. For PD_f the correlation disappeared ($r = 0.43$, $p = 0.13$), and a significant negative correlation (r = -0.43, $p = 0.01$) was observed for PD_r. Scatter plots for f and PD_f are shown in Figure 5.5 for both T_1 black holes and T_2-weighted lesions.

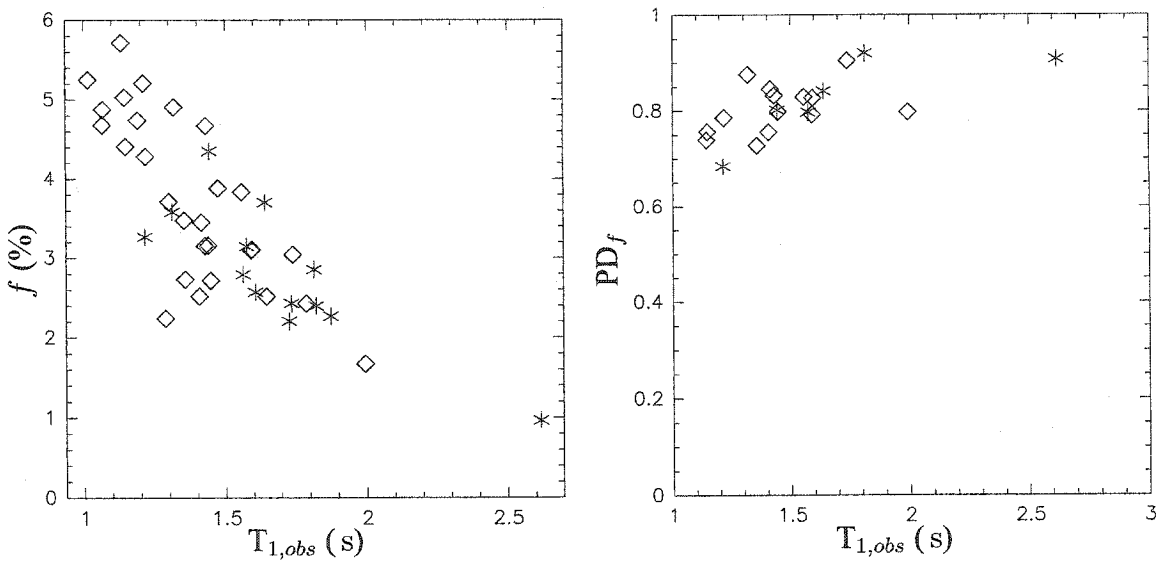

Figure 5.5: f and PD_f as a function of $T_{1,obs}$ for T_1 black holes ($*$) and all T_2 lesions ($\diamond$).

In summary, qMTI parameter estimates have been presented for seven healthy controls, and ten MS patients. These results will be discussed in the next chapter, focusing on the highlights of these findings. Measurements in healthy controls will be used for study validation, and for comparison with values in MS. Results in MS have been categorized into two categories – normal-appearing tissue, and lesions – and findings in both will be discussed.

Chapter 6

Discussion

The previous chapter presented results of data collection and quantitative parameter estimation in seven healthy controls and ten MS patients. Healthy tissue and normal-appearing tissue of MS patients were compared, as well as lesions observed in these patients. Some key parameters were also tested for correlations in order to explore the dependency of exchange rate on macromolecular pool size, and the involvement of the different qMTI parameters in the composition of MTR.

This discussion focuses on a number of issues, beginning with validation of the current measurements. Regional variations of parameter values in healthy controls and normal-appearing tissue of patients are discussed and compared. The role of qMTI parameters involved in the composition of MTR are investigated in tissue and lesions. The chapter closes by considering the interpretation of T_1 hypointensity observations in lesions.

6.1 Validation

The results in healthy controls can provide validation of the current measurements relative to previous studies. Sled and Pike [71] had previously published values in frontal white matter of two subjects, as well as in the caudate nucleus of the first and the cortical grey matter of the second (see Table 3.1). Comparison of these values to the results in this thesis showed the following differences. One must consider that this study involved a greater number of subjects and that comparisons with [71] should be regarded in this light.

In frontal white matter, this work comparatively underestimated f and $T_{2,f}$, while obtaining similar results for k_f, $T_{2,r}$, and $R_{1,f}$. In grey matter, the differences were much slighter though still present. In the caudate nucleus, present estimates of k_f were smaller than those in [71], while similar values were obtained on all other parameters. In cortical grey matter, the difference occurred as a lower estimate of $T_{2,f}$ in this work. In general, measurements appear more stable in grey matter, where MT is less prominent. In white matter, the noisiest estimate is k_f.

These differences can likely be attributed to two main factors. First, the modification of the protocol as described in Section 4.1 influenced estimates of pool size and exchange rate: the shorter MT pulse duration provided less MT saturation, causing increased variance in the estimates of the closely tied parameters f and k_f. The precision on the estimate of k_f also depends strongly on the use of two distinct MT pulse durations, T_{MT}, and the difference between the two values. Given that this spread was reduced in the modifications brought to the current experimental technique, a less stable measurement of k_f was expected. Second, poor fitting of the model to the data near resonance has strongly influ-

enced estimates of $T_{2,f}$, as it is the parameter most responsible for the shape of the model curves near resonance. This has resulted in significant underestimation of $T_{2,f}$.

In the same work [71], values were also published for a single MS patient (see Table 3.2), in frontal white matter, cortical grey matter, as well as two lesions. Comparison of these normal-appearing WM and GM values to the current estimates demonstrated underestimation of f and $T_{2,f}$, while yielding very similar values of k_f, $R_{1,f}$, and $T_{2,r}$. In the cortical grey matter of MS patients, current estimates of f, k_f, $R_{1,f}$, and $T_{2,r}$ were similar to those of Sled and Pike, while $T_{2,f}$ was significantly underestimated. The discrepancies in MS patients between the current results and those previously published are consistent with observations in normals, and can thus be attributed to the observed systematic differences in the protocol. However, comparison with a single MS subject is of little validity.

Finally, Sled and Pike had published values in two lesions of a single MS patient – a young (1-9 months) lesion, and an older (21+ months) lesion. Given that none of the lesions encountered in this study were as young as nine months, the mean measurements for T_2-weighted lesions were compared to those in lesion 2 form Table 3.2. Greater differences were observed in the case of lesions. These are attributed to the much greater variability in parameter values observed in lesions. These differences are even harder to interpret given the low number of comparison values and the expected heterogeneity of MS lesions.

The discrepancies in estimation of $T_{2,f}$ can be further explored by comparing it to measurements of the apparent spin-spin relaxation time constant, $T_{2,obs}$. One would expect estimates of the free pool transverse relaxation rate $T_{2,f}$ to be reflected in $T_{2,obs}$, as this latter value is made up of liquid components only (combining extra- and intracellular water pools). Unfortunately, results for $T_{2,obs}$ and $T_{2,f}$ are nowhere near each other in normals

(*i.e.* in white matter, respectively 82.3 $\pm$ 2.4 ms versus 27.2 $\pm$1.5 ms). The apparent T_2 measurement is believed to be more accurate, while the free pool T_2 value is thought to be largely underestimated, due to poor fitting of the model near resonance.

6.2 Regional variations in controls and patients

In normal controls, no significant left/right differences were observed in qMTI parameters. Most parameters revealed highly significant regional variations: only the free pool proton density PD_f did not show significant differences between regions. Only when considering global tissue type values (*i.e.* WM vs. GM) were differences demonstrated in PD_f. Thus observations of water content were relatively constant among regions in this control group.

Given our observations in the control group, an interpretation may be ventured pertaining to the meaning of certain quantitative measures. Free pool proton density PD_f reflects water content: it may serve in MS as a measure of edema in lesions and will help in the interpretation of the confounding effects of edema in MTR measures. Lesions showed significantly increased PD_f, indicating greater water content. The macromolecular content of tissue is measured by the absolute proton density of the restricted pool, PD_r. Lesions also demonstrated significantly decreased restricted proton density. PD_f was mostly constant across regions of controls and normal-appearing ROIs of patients, and so restricted pool size is reflected in the fractional pool size f ($= PD_r/PD_f$) as well. Given the correlations observed in Sections 5.1.2 and 5.2.2, k_f clearly depends on measures of semi-solid and liquid pool sizes. However, it is likely that k_f may also reflect tissue structure and molecular organization, factors which would influence the rate at which magnetization is exchanged.

In general, the regional variations of qMTI parameters in white matter reflect the point of view that absolute restricted pool proton density PD_r and fractional pool size f correlate strongly with myelination. The large values observed in the corpus callosum and forceps coincide with the presence of tightly packed, heavily myelinated fibers present in this region linking the hemispheres. Also, the larger values observed in the frontal lobe may be tied to the presence of motor fibers, absent in the occipital lobe. Grey matter structures demonstrated much smaller values, consistent with the reduced presence of macromolecules in general and myelin specifically.

In normal-appearing tissue of MS patients, most parameters demonstrated highly significant differences between some regions, with the notable exceptions of $R_{1,f}$ and PD_r. This was attributed to the greater variance observed in the measures for normal-appearing tissue of MS patients, linked to the diffuse pathological changes happening in MS.

Parameter estimates of normal-appearing tissue of patients and healthy tissue in controls were also compared. A two-way ANOVA revealed significant differences between the two groups, and among white matter regions-of-interest, but not grey matter. Subsequent t-tests revealed the significant differences in fractional macromolecular content to be present in the genu and splenium of the corpus callosum and forceps, and in occipital white matter as well. The corpus callosum is a heavily myelinated area of normal white matter and may be changing the most in the disease. The lack of difference between healthy controls and normal-appearing grey matter structures in MS patients indicates that either no change is going on in grey matter, or that they are too slight to be detected with this method.

Interestingly, no difference was observed in PD_f of healthy control and MS normal-appearing regions, implying that water content does not vary from healthy tissue to MS

normal-appearing tissue. This is a particularly interesting point in light of the fact that PD_r and MTR are significantly reduced in normal-appearing white matter of MS patients. It indicates that the widely observed MTR abnormalities in normal-appearing white matter of patients reflect decreased macromolecular content, not diffuse increases in water content.

6.3 Exchange rate dependence on pool sizes

The rate of magnetization transfer between the two pools likely depends on more than just absolute and relative macromolecular tissue content. When considering all regions of all subjects to account for inter-subject variability, k_f was found to correlate only with the fractional pool size f, in both grey and white matter of patients and controls. In the group of patients, k_f correlated with macromolecular pool size f, just as in the control group. k_f and absolute proton density measures were mostly uncorrelated. Furthermore, the relationship between k_f and f appears to become weaker in both groups as f increases (see Fig. 5.1). This could reflect other effects, such as organization, on the exchange rate occurring in regions of high macromolecular concentration.

When considering the rate of magnetization exchange in lesions, k_f did not correlate in any general way with pool size measures f, PD_r, and PD_f, in all lesion types. However, k_f did correlate with f in the T_2-only subset of lesions, probably a reflection of the transitional nature of these lesions between normal-appearing tissue and more the severe tissue destruction expected in T_1-hypointense lesions. Recalling that the exchange rate was moderately linked to macromolecular fraction both in controls and normal-appearing tissue of patients, this difference may demonstrate that there could be modification in tissue

arrangements during the evolution of lesions independent of simple tissue loss.

Any change in macromolecular content will likely affect the exchange rate, but the lack of correlation between the exchange rate and absolute proton density measures may indicate that other structural factors play a more important role in determining k_f. This implies that while content is reflected in f, PD_r, and PD_f, k_f is also determined by tissue organization. Naturally, content and structural organization are correlated in biological tissue, particularly in healthy tissue, but macromolecular organization is likely to affect the exchange process. In MS, there may be an independent change in the rate due to factors other than tissue loss, based on the moderate correlation seen on an individual basis. One might speculate that this change occurs because of re-organization or breakdown of tissue before it is removed.

6.4 Role of qMTI parameters in MTR

MTR has long been the most common way of characterizing the MT effect in tissue. It has revealed focal changes in pre-lesional tissue, but is limited in its view by the fact that it combines multiple aspects of relaxation and magnetization exchange into a single parameter. In the control group, MTR was observed to correlate moderately with many qMTI parameters in white matter. This supports the belief that the semi-quantitative measure of MTR does indeed reflect a combination of parameters rather than simply restricted pool size, as it has sometimes been simplistically interpreted.

Observations in this control group indicated that exchange rate and MTR depend mostly on the macromolecular fraction. Nonetheless, this does not lead to a direct relationship,

and suggests that most of the quantitative parameters need to be considered in analysis of pathological tissue. As hypothesized, the free pool longitudinal relaxation rate does play a role in MTR, as $R_{1,f}$ correlates significantly with MTR in this group of controls. In the normal-appearing tissue of patients, no differences from controls were observed in the link between MTR and the qMTI parameters, with the exception of one parameter, $T_{2,r}$. It demonstrated a correlation with MTR that suggests that, while $T_{2,r}$ does not play a direct role in MTR, some changes in tissue content are reflected in both of these parameters. he meaning of this finding, observed only in patients, remains unclear.

The dependence of MTR on qMTI parameters was also studied in these lesions. A strong correlation was observed between MTR and f in T_1-weighted lesions, possibly indicating that these lower MTR values largely reflect changes in macromolecular content in these destructive lesions. The slightly weaker correlation noted for T_2 lesions leads us to believe that this is less true of more inflammatory lesions and higher MTR values. The correlation observed between MTR and k_f in T_2 lesion voxels supports the hypothesis that tissue reorganization may be occuring prior to removal of macromolecular components.

The large spread observed in f in the upper range MTR values – a two-fold difference was observed in f for MTR values in the range of 35 - 45 % – reflects possible changes in the exchange mechanism, properties of free pool, and $R_{1,f}$ relaxation constant, all in addition to the known change in semi-solid/liquid fraction. Together, these results suggest that, as hypothesized, moderate decreases in MTR, often measured in younger lesions, reflect more than a simple decrease in the macromolecular pool size. Therefore, the fractional pool size f likely provides a measurement more specific to demyelination in these acute lesions.

6.5 T_1 hypointensities

In lesions described as T_1 black holes, it is generally believed that the increase in $T_{1,obs}$, which causes them to appear as hypointensities on clinical T_1-weighted scans, corresponds to a drop in the size of the restricted pool. This drop is directly related to a loss of tissue structure integrity and hence, myelin. However, confirmation of this destructive characteristic may be confounded by the presence of inflammation and edema.

The findings that $T_{1,obs}$ correlated with f and PD_r, but not PD_f, confirmed that the drop in T_1 is in fact related to the loss of restricted pool size. Furthermore, the effect of changes in free pool proton density, as measured by PD_f, had little or no effect on signal intensity. Therefore, the view that black holes are highly demyelinated lesions is supported. Increased liquid pool size, through inflammation and edema, is observed to play a much lesser role in T_1 hypointensity.

It is noted, however, that MTR showed a stronger link to fractional pool size than did $T_{1,obs}$, and was unaffected by changes in free pool proton density in T_1 lesions. Thus, MTR should offer a more direct view on myelination and tissue content in general than measurement of the apparent T_1.

Chapter 7

Conclusion and Future Work

This thesis presented a cross-sectional study of healthy controls and MS patients performed using the novel technique of quantitative magnetization transfer imaging. The objectives were to extend the knowledge about changes observed in MS, while furthering the understanding of established clinical exam methods. We have reported on normal values of qMTI parameters in healthy controls, most importantly to serve as a reference for future work and comparison with pathological values. Parameter estimates have also been presented in MS patients, for both normal-appearing tissue and clinically observable lesions.

Regional variations were observed in both healthy controls and MS patients, especially in white matter. Notably, the liquid pool proton density was relatively constant within tissue types. Most of our measures also demonstrated differences between the normal-appearing white matter in MS and healthy white matter, with once again the notable exception of absolute liquid pool size. Water content was found to be a very stable quantity in both healthy and normal-appearing white matter.

In grey matter, the results did not indicate any distinction between patients and controls. Though this may be a shortcoming of this limited study, the thorough examination and exclusion of partial voluming effects in considering grey matter regions suggest that this method may not detect changes that might be occurring in grey matter. On the other hand, it is possible that changes are not occurring in the normal-appearing grey matter of patients.

Investigations were made into the relationship between magnetization exchange rate and macromolecular pool size in tissue. It is believed that the rate at which exchange of magnetization occurs depends on more than just macromolecular tissue content. Structure and organization should be involved as well. The findings reported show that a direct link cannot be established between rate of exchange and tissue content, especially in MS lesions.

More importantly, this thesis wanted to explore the combination of parameters that are believed to play a dominant role in the magnetization transfer ratio, potentially leading to confounding effects. The findings supported the notion that the main factor involved in MTR is the fractional pool size, which measures the size of the restricted pool to that of the free pool. When coupled to the finding that the free pool proton density is relatively constant in normals and MS patients, this suggests that MTR abnormalities seen in normal-appearing white matter of MS patients reflect macromolecular change rather than increased water content. Other important factors that were suggested to play a role in the MTR were the exchange rate k_f and the free pool longitudinal relaxation rate $R_{1,f}$. In T_2 lesions, k_f was still observed to play a role in MTR, while in T_1 "black holes", the MTR depended mostly on tissue content.

Finally, the ability of T_1-weighted scans – and the hypointense lesions observed in

them – to demonstrate significant tissue destruction was also examined . It was found that apparent T_1 correlated with macromolecular pool size quite strongly, thus confirming the belief that T_1 hypointensities reflect advanced tissue loss via destructive lesions. The confounding effects of inflammation and edema were not observed to play a significant role in producing T_1 hypointense lesions.

Much work remains to be done using this relatively new technique. Further comparison of the current single-slice qMTI technique with MTR imaging should be performed, with more subjects. Care should be taken in the selection of patients, in order to expand the range of data to include new lesions, and possibly other areas of the cerebrum. Longitudinal studies of patients will provide temporal and disease progression data.

Development of an improved experimental methodology – ideally providing whole-head, high-resolution qMTI, MTR and relaxometry parameter estimate maps, with field inhomogeneity corrections – is key to the advancement of our understanding of MT in CNS tissue. Other aspects of quantitative imaging, notably multi-component T_2 relaxometry, will contribute greatly to the understanding and modeling of tissue development, structure, and pathology. This will require implementation of a volumetric multi-component T_2 measurement and analysis method, to be incorporated into a complete quantitative experimental technique.

Investigation of the model describing magnetization exchange in tissue should be pursued, along with the compartmentalization of water, in an effort to reconcile the two-pool model of MT and the multiple water compartment model of T_2 relaxometry. Quantitative diffusion imaging could potentially be useful in the study of this water compartmentalization issue.

With a sound technique in hand, whole-head and/or high-resolution qMTI studies in healthy controls and MS patients could be performed to help refine the results and conclusions presented in this thesis. Other pathologies, such as cortical dysplasia, Alzheimer's disease, and other degenerative diseases, could also be explored, as well as studying normal brain development.

Appendix A

Ethics Approval

A copy of the ethics approval letter from the Research Ethics Board of McGill University, for the qMTI study of multiple sclerosis at the Montreal Neurological Institute, is included.

Recd. June 26/01

Centre universitaire de santé McGill
McGill University Health Centre

27 June 2001

Dr Bruce Pike
Magnetic Resonance Imaging
MNI

Meeting of 2001.06.26
3.k. PIKB 1995/2 **Quantitative Magnetization Transfer Imaging of Multiple Sclerosis (CIHR)**
Documentation: Letter of 2001.06.14, Checklist, English and French consent forms (signature pages of both dated 2001.06)

The board approves renewal of the above protocol and accompanying consent forms for a period of one year.

Yours very truly,

Ronald Pokrupa, MD, Chair
Research Ethics Board
/ve

L'HÔPITAL NEUROLOGIQUE DE MONTRÉAL • MONTREAL NEUROLOGICAL HOSPITAL
3801, rue University, Montréal (Québec) H3A 2B4 Tél.: (514) 398-6644

Bibliography

[1] E. M. Purcell, H. C. Torrey, and R. V. Pound, "Resonance absorption by nuclear magnetic moments in a solid," *Physical Review*, vol. 69, pp. 37–38, 1946.

[2] F. A. Bloch, "Nuclear induction," *Physical Review*, vol. 70, pp. 460–474, 1946.

[3] P. C. Lauterbur, "Image formation by induced local interactions: Examples employing NMR," *Nature*, vol. 242, pp. 190–191, 1973.

[4] R. Damadian, "Tumor detection by nuclear magnetic resonance," *Science*, vol. 171, pp. 1151–1153, March 1971.

[5] E. M. Haacke, R. W. Brown, M. R. Thompson, and R. Venkatesan, *Magnetic resonance imaging: physical principles and sequence design*. New York: John Wiley & Sons, 1999.

[6] D. G. Nishimura, *Principles of Magnetic Resonance Imaging*. Stanford, California: Stanford University, 1996.

[7] J. M. Charcot, "Histologie de la sclérose en plaques," *Gaz Hop civils et militaires*, vol. 140, 141, 143, pp. 554–555, 557–558, 566, 1868.

[8] A. Compston and A. Coles, "Multiple sclerosis," *The Lancet*, vol. 359, pp. 1221–1231, April 2002.

[9] J. H. Noseworthy, C. Lucchinetti, M. Rodriguez, and B. G.Weinshenker, "Multiple sclerosis," *New England Journal of Medicine*, vol. 47, no. 6, pp. 707–717, 2000.

[10] L. Steinman, "Multiple sclerosis: a two-stage disease," *Nature Immunology*, vol. 2, pp. 762–764, September 2001.

[11] P. Rieckmann and K. J. Smith, "Multiple sclerosis: more than inflammation and demyelination," *Trends in Neuroscience*, vol. 24, pp. 435–437, August 2001.

[12] C. Lucchinetti, W. Brück, J. Parisi, B. Scheithauer, M. Rodriguez, and H. Lassmann, "Heterogeneity of multiple sclerosis lesions: Implications for the pathogenesis of demyelination," *Annals of Neurology*, vol. 47, no. 6, pp. 707–717, 2000.

[13] S. G. Waxman, "Multiple sclerosis as a neuronal disease," *Archives of Neurology*, vol. 57, pp. 22–24, January 2000.

[14] D. Kidd, F. Barkhof, R. McConnell, P. R. Algra, I. V. Allen, and T. Revesz, "Cortical lesions in multiple sclerosis," *Brain*, vol. 122, pp. 17–26, 1999.

[15] B. Hemmer, J. J. Archelos, and H.-P. Hartung, "New concepts in the immunopathogenesis of multiple sclerosis," *Nature Neuroscience*, vol. 3, pp. 291–301, April 2002.

[16] D. M. Wingerchuk, C. F. Lucchinetti, and J. H. Noseworthy, "Multiple sclerosis: Current pathophysiological concepts," *Laboratory Investigation*, vol. 81, pp. 263–281, 2001.

[17] K. J. Smith and W. I. McDonald, "The pathophysiology of multiple sclerosis: the mechanisms underlying the production of symptoms and the natural history of the disease," *Philosophical Transactions of the Royal Society of London*, vol. 354, pp. 1649–1673, 1999.

[18] C. M. Poser, D. W. Paty, L. Scheinberg, W. I. McDonald, F. A. Davis, G. C. Ebers, K. P. Johnson, W. A. Sibley, D. H. Silberberg, and W. W. Tourtellotte, "New diagnostic criteria for multiple sclerosis: guidelines for research protocols," *Annals of Neurology*, vol. 13, pp. 227–231, March 1983.

[19] W. I. McDonald, A. Compston, G. Edan, D. Goodkin, H.-P. Hartung, F. D. Lublin, H. F. McFarland, D. W. Paty, C. H. Polman, S. C. Reingold, M. Sandberg-Wollheim, W. Sibley, A. Thompson, S. van den Noort, B. Y. Weinshenker, and J. S. Wolinsky, "Recommended diagnostic criteria for multiple sclerosis: Guidelines from the International Panel on the Diagnosis of Multiple Sclerosis," *Annals of Neurology*, vol. 50, pp. 121–127, 2001.

[20] J. F. Kurtzke, "Disability rating scales in multiple sclerosis," *Annals of the New York Academy of Sciences*, vol. 436, no. 1, pp. 347–360, 1984.

[21] B. M. Keegan and J. H. Noseworthy, "Multiple sclerosis," *Annual Review in Medicine*, vol. 53, pp. 285–302, 2002.

[22] D. H. Miller, R. I. Grossman, S. C. Reingold, and H. F. McFarland, "The role of magnetic resonance techniques in understanding and managing multiple sclerosis," *Brain*, vol. 121, pp. 3–24, 1998.

[23] F. Fazekas, F. Barkhof, M. Filippi, R. I. Grossman, D. K. B. Li, W. I. McDonald, H. F. McFarland, D. W. Paty, J. H. Simon, J. S. Wolinsky, and D. H. Miller, "The contribution of magnetic resonance imaging to the diagnosis of multiple sclerosis," *Neurology*, vol. 53, pp. 448–456, 1999.

[24] M. Filippi and R. I. Grossman, "MRI techniques to monitor MS evolution. The present and the future," *Neurology*, vol. 58, pp. 1147–1153, 2002.

[25] D. L. Arnold and P. M. Matthews, "MRI in the diagnosis and management of multiple sclerosis," *Neurology*, vol. 58, pp. S23–S31, 2002.

[26] J. I. O'Riordan, A. J. Thompson, D. P. E. Kingsley, D. G. MacManus, B. E. Kendall, P. Rudge, W. I. McDonald, and D. H. Miller, "The prognostic value of brain MRI in clinically isolated syndromes of the CNS: A 10-year follow-up," *Brain*, vol. 121, pp. 495–503, 1998.

[27] M. Rovaris, G. Comi, and M. Filippi, "The role of non-conventional MR techniques to study multiple sclerosis patients," *Journal of the Neurological Sciences*, vol. 186, pp. S3–S9, 2001.

[28] M. A. van Walderveen, W. Kamphorst, P. Scheltens, J. van Waesberghe, R. Ravid, J. Valk, C. Polman, and F. Barkhof, "Histopathologic correlates of hypointense lesions on T_1-weighted spin-echo MRI in multiple sclerosis," *Neurology*, vol. 50, pp. 1282–1288, 1998.

[29] J. F. Hiehle, R. I. Grossman, K. N. Ramer, F. Gonzales-Scarano, and J. A. Cohen, "Magnetization transfer effects in MR-detected multiple sclerosis lesions: compari-

son with gadolinium-enhanced spin-echo images and nonenhanced T_1-weighted images," *American Journal of Neuroradiology*, vol. 16, pp. 69–77, 1995.

[30] L. A. Loevner, R. I. Grossman, J. C. McGowan, K. N. Ramer, and J. A. Cohen, "Characterization of multiple sclerosis plaques with T_1-weighted MR and quantitative magnetization transfer," *American Journal of Neuroradiology*, vol. 16, pp. 1473–1479, 1995.

[31] M. Filippi, T. Yousry, A. Campi, C. Kandziora, B. Colombo, R. Voltz, V. Martinelli, S. Spuler, S. Bressi, G. Scotti, and G. Comi, "Comparison of triple dose versus standard dose gadolinium-DTPA for detection of MRI enhancing lesions in patients with MS," *Neurology*, vol. 46, pp. 379–384, 1996.

[32] N. C. Silver, C. D. Good, G. J. Barker, D. G. MacManus, A. J. Thompson, I. F. Moseley, W. I. McDonald, and D. H. Miller, "Sensitivity of contrast enhanced MRI in multiple sclerosis. effects of gadolinium dose, magnetisation transfer contrast and delayed imaging," *Brain*, vol. 120, pp. 1149–1161, 1997.

[33] I. Kay and R. Henkelman, "Practical implementation and optimization of one-shot T_1 imaging," *Magnetic Resonance in Medicine*, vol. 22, no. 1, pp. 414–424, 1991.

[34] C. S. Poon and R. M. Henkelman, "Practical T_2 quantitation for clinical applications," *Journal of Magnetic Resonance Imaging*, vol. 2, pp. 541–553, Sep-Oct 1992.

[35] D. Lacomis, D. Osbakken, and G. Gross, "Spin-lattice relaxation (T_1) times of cerebral white matter in multiple sclerosis," *Magnetic Resonance in Medicine*, vol. 3, no. 2, pp. 194–202, 1986.

[36] L. Rumbach, J. P., Armspach, D. Gounot, I. J. Namer, J. Chambron, J. M. Warter, and M. Collard, "Nuclear magnetic resonance T_2 relaxation times in multiple sclerosis," *Journal of Neurological Science*, vol. 104, pp. 176–181, 1991.

[37] K. Gersonde, T. Tolxdorff, and L. Felsberg, "Identification and characterization of tissues by T_2-selective whole-body proton NMR imaging," *Magnetic Resonance in Medicine*, vol. 2, pp. 390–401, 1985.

[38] R. S. Menon and P. S. Allen, "Application of continuous relaxation time distributions to the fitting of data from model systems and excised tissue," *Magnetic Resonance in Medicine*, vol. 20, pp. 214–227, 1991.

[39] A. MacKay, K. Whitall, J. Adler, D. Li, D. Paty, and D. Graeb, "In vivo visualization of myelin water in brain by magnetic resonance," *Magnetic Resonance in Medicine*, vol. 31, pp. 673–677, Jun 1994.

[40] K. Whitall, A. MacKay, D. Graeb, N. R., , D. Li, and D. Paty, "*In vivo* measurement of T_2 distributions and water contents in normal human brain," *Magnetic Resonance in Medicine*, vol. 37, pp. 34–43, 1997.

[41] D. LeBihan, R. Turner, J. Pekar, and C. T. W. Moonen, "Diffusion and perfusion imaging by gradient sensitization: design, strategy and significance," *Journal of Magnetic Resonance Imaging*, vol. 1, pp. 7–28, 1991.

[42] M. A. Horsfield, M. Lai, S. L. Webb, G. J. Barker, P. S. Tofts, R. Turner, P. Rudge, and D. H. Miller, "Apparent diffusion coefficients in benign and secondary progressive

multiple sclerosis by nuclear magnetic resonance," *Magnetic Resonance in Medicine*, vol. 36, pp. 393–400, 1996.

[43] R. Bammer, M. Augustin, S. Strasser-Fuchs, T. Seifert, P. Kapeller, R. Stollberger, F. Ebner, H.-P. Hartung, and F. Fazekas, "Magnetic resonance diffusion tensor imaging for characterizing diffuse and focal white matter abnormalities in multiple sclerosis," *Magnetic Resonance in Medicine*, vol. 44, pp. 583–591, October 2000.

[44] P. M. Matthews, N. D. Stefano, S. Narayanan, G. S. Francis, J. S. Wolinsky, J. P. Antel, and D. L. Arnold, "Putting magnetic resonance spectroscopy studies in context: axonal damage and disability in multiple sclerosis," *Seminars in Neurology*, vol. 18, pp. 327–336, 1998.

[45] T. L. Richards, "Proton MR spectroscopy in multiple sclerosis: value in establishing diagnosis, monitoring progression, and evaluating therapy [Review]," *American Journal of Roentgenology*, vol. 157, pp. 1073–1078, 1991.

[46] N. D. Stefano, P. M. Matthews, J. P. Antel, M. Preul, G. S. Francis, and D. L. Arnold, "Chemical pathology of acute demyelinating lesions and its correlation with disability," *Annals of Neurology*, vol. 38, no. 38, pp. 901–909, 1995.

[47] C. A. Davie, G. J. Barker, S. Webb, P. S. Tofts, A. J. Thompson, A. E. Harding, W. I. McDonald, and D. H. Miller, "Persistent functional deficit in multiple sclerosis and autosomal dominant cerebellar ataxia is associated with axon loss [published erratum appears in Brain 1996 Aug;119(Pt 4):1415]," *Brain*, vol. 118, no. 6, pp. 1583–1592, 1995.

[48] H. Reddy, S. Narayanan, R. Arnoutelis, M. Jenkinson, J. Antel, P. Matthews, and D. Arnold, "Evidence for adaptive functional changes in the cerebral cortex with axonal injury from multiple sclerosis," *Brain*, vol. 123, pp. 2314–2320, 2000.

[49] M. Lee, H. Reddy, H. Johansen-Berg, S. Pendlebury, M. Jenkinson, S. Smith, J. Palace, and P. Matthews, "The motor cortex shows adaptive functional changes to brain injury from multiple sclerosis.," *Annals of Neurology*, vol. 47, pp. 606–613, 2000.

[50] J. Thorpe, S. Halpin, D. MacManus, G. Barker, B. Kendall, and D. Miller, "A comparison between fast and conventional spin-echo in the detection of multiple sclerosis lesions," *Neuroradiology*, vol. 36, pp. 388–392, 1994.

[51] N. Evangelou, M. M. Esiri, S. Smith, J. Palace, and P. M. Matthews, "Quantitative pathological evidence for axonal loss in normal-appearing white matter in multiple sclerosis," *Annals of Neurology*, vol. 47, pp. 391–395, 2000.

[52] C. Liu, S. Edwards, Q. Gong, N. Roberts, and L. D. Blumhardta, "Three-dimensional MRI estimates of brain and spinal cord atrophy in multiple sclerosis," *Journal of Neurology, Neurosurgery, and Psychiatry*, vol. 66, pp. 323–330, 1999.

[53] N. A. Losseff, L. Wang, H. M. Lai, D. S. Yoo, M. L. Gawne-Cain, W. I. McDonald, D. H. Miller, and A. J. Thompson, "Progressive cerebral atrophy in multiple sclerosis. a serial MRI study," *Brain*, vol. 119, pp. 2009–2019, 1996.

[54] J. T. Chen, S. M. Smith, D. L. Arnold, and P. M. Matthews, "Quantification of change in cortical grey matter thickness in multiple sclerosis," in *Proc. 10th Int. Soc. Mag. Res. Med.*, p. 351, 2002.

[55] W. Kucharczyk, P. M. Macdonald, G. J. Stanisz, and R. M. Henkelman, "Relaxivity and magnetization transfer of white matter lipids at MR imaging: importance of cerebrosides and pH," *Radiology*, vol. 192, pp. 521–529, 1994.

[56] S. H. Koenig, R. D. Brown, M. Spiller, and N. Lundbom, "Relaxometry of brain: Why white matter appears bright in MRI," *Magnetic Resonance in Medicine*, vol. 14, no. 3, pp. 482–495, 1990.

[57] V. Dousset, R. I. Grossman, K. N. Ramer, M. D. Schnall, L. H. Young, F. Gonzalez-Scarano, E. Lavi, and J. A. Cohen, "Experimental allergic encephalomyelitis and multiple sclerosis: lesion characterization with magnetization transfer imaging," *Radiology*, vol. 182, pp. 483–491, 1992.

[58] M. Filippi, M. A. Rocca, G. Martino, M. A. Horsfield, and G. Comi, "Magnetization transfer changes in the normal-appearing white matter precede the appearance of enhancing lesions in patients with multiple sclerosis," *Annals of Neurology*, vol. 43, pp. 809–814, 1998.

[59] G. B. Pike, N. De Stefano, S. Narayanan, K. J. Worsley, D. Pelletier, G. S. Francis, J. P. Antel, and D. L. Arnold, "Multiple sclerosis: magnetization transfer MR imaging of white matter before lesion appearance on T_2-weighted images," *Radiology*, vol. 215, pp. 824–830, June 2000.

[60] R. S. Balaban and T. L. Ceckler, "Magnetization transfer contrast in magnetic resonance imaging," *Magnetic Resonance Quarterly*, vol. 8, pp. 116–137, Jun 1992.

[61] G. E. Santyr and R. V. Mulkern, "Magnetization transfer in MR imaging," *Journal of Magnetic Resonance Imaging*, vol. 5, pp. 121–124, Jan-Feb 1995.

[62] R. M. Henkelman, G. J. Stanisz, and S. J. Graham, "Magnetization transfer in MRI: a review," *NMR in Biomedicine*, vol. 14, no. 1, pp. 57–64, 2001.

[63] H. T. Edzes and E. D. Samulski, "Cross relaxation and spin diffusion in the proton NMR of hydrated collagen," *Nature*, vol. 265, pp. 521–523, 1977.

[64] G. B. Pike, "Magnetization transfer imaging of multiple sclerosis - Workshop on new MR techniques in clinical neurosurgery," *Italian Journal of Neurological Science*, vol. 18, no. 1, pp. 359–365, 1997.

[65] S. D. Wolff and R. S. Balaban, "Magnetization transfer contrast (MTC) and tissue water proton relaxation *in vivo*," *Magnetic Resonance in Medicine*, vol. 10, no. 1, pp. 135–144, 1989.

[66] S. D. Wolff, J. Eng, and R. S. Balaban, "Magnetization transfer contrast: Method for improving contrast in gradient-recalled-echo images," *Radiology*, vol. 179, pp. 133–137, 1991.

[67] B. S. Hu, S. M. Conolly, G. A. Wright, D. G. Nishimura, and A. Macovski, "Pulsed saturation transfer contrast," *Magnetic Resonance in Medicine*, vol. 26, no. 2, pp. 231–240, 1992.

[68] S. J. Graham and R. M. Henkelman, "Pulsed magnetization transfer imaging: Evaluation of technique," *Radiology*, vol. 212, pp. 903–910, September 1999.

[69] G. B. Pike, G. H. Glover, B. S. Hu, and D. R. Enzmann, "Pulsed magnetization transfer spin-echo MR imaging," *Journal of Magnetic Resonance Imaging*, vol. 3, pp. 531–539, May-Jun 1993.

[70] J. Eng, T. I. Ceckler, and R. S. Balaban, "Quantitative ^{1}H magnetization transfer imaging *in vivo*," *Magnetic Resonance in Medicine*, vol. 17, no. 2, pp. 304–314, 1991.

[71] J. G. Sled and G. B. Pike, "Quantitative imaging of magnetization transfer exchange and relaxation properties *in vivo* using MRI," *Magnetic Resonance in Medicine*, vol. 46, no. 5, pp. 923–931, 2001.

[72] G. B. Pike, B. S. Hu, G. H. Glover, and D. R. Enzmann, "Magnetization transfer time-of-flight magnetic resonance angiography," *Magnetic Resonance in Medicine*, vol. 25, pp. 372–9, Jun 1992.

[73] F. Sardanelli, C. Losacco, A. Iozzelli, P. Renzetti, E. Rosso, R. Parodi, M. Bonetti, and M. A., "Evaluation of Gd-enhancement in brain MR of multiple sclerosis: image subtraction with and without magnetization transfer," *European Radiology*, vol. 12, pp. 2077–2082, August 2002.

[74] R. M. Henkelman, X. Huang, Q. S. Xiang, G. J. Stanisz, S. D. Swanson, and M. J. Bronskill, "Quantitative interpretation of magnetization transfer," *Magnetic Resonance in Medicine*, vol. 29, pp. 759–766, Jun 1993.

[75] M. Goldman, *Spin Temperature and Nuclear Magnetic Resoance in Solids*. London: Oxford University Press, 1970.

[76] G. B. Pike, "Pulsed magnetization transfer contrast in gradient echo imaging: A two-pool analytic description of signal response," *Magnetic Resonance in Medicine*, vol. 36, pp. 95–103, Jul 1996.

[77] J. G. Sled and G. B. Pike, "Quantitative interpretation of magnetization transfer in spoiled gradient echo MRI sequences," *Journal of Magnetic Resonance*, vol. 145, pp. 24–36, 2000.

[78] J. G. Sled and G. B. Pike, "Correction for B_1 and B_0 variations in quantitative T_2 measurements using MRI," *Magnetic Resonance in Medicine*, vol. 43, no. 4, pp. 589–593, 2000.

[79] T. E. Skinner and G. H. Glover, "An extended two-point dixon algorithm for calculating separate water, fat, and B_0 images," *Magnetic Resonance in Medicine*, vol. 37, pp. 628–30, Apr 1997.

[80] J. G. Sled, *Quantitative imaging of magnetization transfer exchange and relaxation properties in vivo using MRI*. PhD thesis, McGill University, Montreal, QC, May 2001.

[81] J. G. Sled, I. Levesque, C. Santos, S. J. Francis, S. Narayanan, S. D. Brass, D. L. Arnold, and G. B. Pike, "Regional variations in normal brain shown by quantitative magnetization transfer imaging," in *Proc. 10^{th} Int. Soc. Mag. Res. Med.*, p. 1313, 2002.

[82] I. Levesque, J. G. Sled, S. D. Brass, A. C. Santos, S. Narayanan, S. J. Francis, D. L. Arnold, and G. B. Pike, "Comparison of MTR and qMT imaging of multiple sclerosis lesions," in *Proc. 10th Int. Soc. Mag. Res. Med.*, p. 1183, 2002.

[83] J. G. Sled, I. Levesque, S. Narayanan, C. Santos, S. D. Brass, S. J. Francis, D. L. Arnold, and G. B. Pike, "The role of edema and demyelination in T_1 black holes: a quantitative magnetization transfer study," in *Proc. 10th Int. Soc. Mag. Res. Med.*, p. 181, 2002.